40

COMPRESSIVE HIGH CYCLE AT LOW STRAIN FATIGUE BEHAVIOR OF BOVINE TRABECULAR BONE

by

Deborah Wen-hsin Cheng

S.B. Civil Engineering
Stanford University (1992)

Submitted to the Department of Civil and Environmental Engineering in Partial Fulfillment of the Requirements for the Degree of

MASTER OF SCIENCE
in Civil and Environmental Engineering

at the

MASSACHUSETTS INSTITUTE OF TECHNOLOGY

February 1995

Signature of the author _____
Department of Civil and Environmental Engineering
January 18, 1995

Certified by _____
Lorna J. Gibson, Ph.D.
Associate Professor of Civil and Environmental Engineering
Thesis Supervisor

Accepted by _____
Joseph M. Sussman, Chairman
Departmental Committee on Graduate Studies

COMPRESSIVE HIGH CYCLE AT LOW STRAIN FATIGUE BEHAVIOR OF BOVINE TRABECULAR BONE

by

Deborah Wen-hsin Cheng

Submitted to the Department of Civil and Environmental Engineering on January 18, 1995 in Partial Fulfillment of the Requirements for the Degree of Master of Science in Civil and Environmental Engineering.

ABSTRACT

Micro fatigue damage to bone resulting from repetitive, low-intensity loading of normal activity is believed to play a significant role in stress fractures, bone remodelling, and spontaneous fractures in the elderly, with estimated medical costs of over $1 billion annually. Age-related fractures most frequently occur in trabecular bone sites, such as the vertebral body, the proximal femur, and the distal radius. Thus the compressive fatigue behavior of trabecular bone is important in the understanding of clinical orthopaedic issues.

Fatigue experiments of trabecular bone can result in large data scatter if unintentional off-axis testing occurs. A technique that selects for well-aligned and homogeneous specimens to reduce data scatter has been developed (Keaveny *et al.*, 1994). To validate the specimen selection technique, three-dimensional micro-magnetic resonance images of specimens selected using the technique were obtained and analyzed. Results suggest that the use of contact radiography in selecting specimens ensures that the alignment and density of specimens are of an acceptable level.

The validated technique was then used to select bovine trabecular bone specimens for compressive fatigue tests. Specimens were fatigued under loads corresponding to low stress levels using a test protocol that minimizes experimental artifacts (Keaveny *et al.*, 1994) to accurately characterize the compressive fatigue behavior of trabecular bone. A single linear function relates the log normalized applied stress to the log number-of-cycles-to-failure along the entire normalized stress range tested. The slope of this function lies between those expected from modes of creep and slow crack growth (Guo *et al.*, 1994). The fatigue experiments did not reveal distinct low and high cycle regimes, suggesting that fatigue damage may be caused by some combination of the creep and slow crack growth mechanisms or by additional, as yet unmodelled, mechanisms, such as creep buckling.

Thesis Supervisor: Lorna J. Gibson
Title: Associate Professor, Department of Civil and Environmental Engineering

Acknowledgements

I could not do this alone. In writing this thesis I have received assistance from many people and it is impossible for me to thank them adequately for sharing with me their knowledge of life, love, and bone.

There's no substitute for good help, encouragement, talent, inspiration, and humor--all of which I found at OBL. I am first grateful to Lorna Gibson for her inspiration and judgement as my advisor and mentor. Thank you for looking out for this med-school bound civil engineer. Thanks to Toby Hayes for the opportunity to work at OBL with such wonderful people and resources. Lorna and Toby's encouragement, support, and guidance helped keep the train running.

Thank you to John Hipp, Debbie Burstein, and Alan Jansjuwicz for their expert MRI instruction and advice and especially for their patience at the right times.

Tania Pinilla deserves special mention--the frustrations and successes of the MRI study were equally shared with her. A true blue friend-- I owe a debt of gratitude to her.

Special thanks to Quang Pham for his extensive e-mail and FAX conversations, Betsy Myers, and Michael Harrington--all who helped me make sense of my statistical and computer thoughts.

Dan Michaeli provided AVS and MRI data analysis assistance and Aaron Hecker supplied Instron instruction for which I am very thankful.

I certainly want to thank the t-bone group and especially Tony, Ed W., Stevie B.,

Matt, Em, Catherine, Aya, Stefan, Meredith, Jeanine, and Paula for their special talents and positive spirit. Long after Ed Guo moved on to Michigan and I had adopted his fatigue study baby, he continued to provide support and feedback to my pesky email--thank you.

Writing this thesis required an enormous amount of help from friends. Thanks to Craig who promised to help and he did. His humor and wisdom and Jeano's humorous wisdom kept me laughing. Thank you for letting me be me and expanding my understanding and ability to honour hockey. Thanks also to Eric and Carey. I could not ask for better friends.

Finally, thank you to Mom and Dad, and George and Annie for teaching me the important things in life and motivating me to higher achievements. Their love, wisdom, and strength continue to inspire me.

A person cannot clap with one hand. Thank you for a year filled with applause.

孤掌難鳴

Table of Contents

List of Figures

List of Tables

Chapter 1

Introduction: load. . .unload. . .load. . .unload. . .

1.1 Role of fatigue in stress fractures, bone remodelling, and spontaneous fractures

Normal activity such as breathing, walking, lifting objects, rising from a chair, and bending over exposes bone *in vivo* to repetitive, low-intensity loading. Although these cyclic loads produce stress levels lower than those required to fracture a bone specimen under static loading, they can result in damage at the microstructural level (Carter *et al.*, 1981a; Carter and Hayes, 1977a; Schaffler *et al.*, 1989). Not all loads necessarily result in damage to bone; however, microstructural damage in the form of microcracks, microfractures, or microcalli has been observed in individual trabeculae of the lumbar spine (Vernon-Roberts and Pirie, 1973), acetabulum (Ohtani and Azuma, 1984), femoral head (Benaissa *et al.*, 1989; Dunstan *et al.*, 1990; Freeman *et al.*, 1974; McFarland and Frost, 1961; Todd *et al.*, 1972; Urovitz *et al.*, 1977; Wong *et al.*, 1985), and proximal tibia (Pugh *et al.*, 1973a) of post-mortem human specimens. Microstructural damage induced by repetitive loading has been hypothesized to play a significant role in stress fractures (Morris and Blickenstaff, 1967; Devas, 1975; Griffiths *et al.*, 1971), bone remodelling (Pugh *et al.*, 1973b), spontaneous fractures in the elderly (Dunstan *et al.*, 1990, Freeman *et al.*, 1974; Urovitz *et al.*, 1977; Wong *et al.*, 1985), aseptic necrosis of the femoral head (McFarland and Frost, 1961), degenerative joint disease (Radin *et al.*, 1973b, Benaissa *et al.*, 1989), and other bone disorders (Ohtani and Azuma, 1984).

1.1.1 Stress fractures

Fatigue damage accumulation can result from high levels of stress repeated over shorter periods of time and may be the major etiology of stress fractures clinically observed in various anatomic locations (metatarsals, calcaneus, femoral neck

and shaft, tibia, fibula, and spine) in highly active patient populations (military recruits, high performance athletes, and recreational athletes) (Morris and Blickenstaff, 1967; Devas, 1975; Griffiths *et al.*, 1971). Cases of stress fractures generally have the following characteristics:

1) not associated with a single or traumatic event;

2) associated with activities involving repetitive loading of the involved bone;

3) preceded by symptoms of impending fracture (joint tenderness and swelling) without radiographic evidence of fracture;

4) symptoms subside while at rest for a period of time;

5) if radiographic signs are seen they are in the form of a fracture line or associated with callus formation;

6) if stress fractures occur they are in the form of blunt, brittle fracture planes (Nunamaker *et al.*, 1990).

Stress fractures were first clinically reported in 1865 by army surgeons who observed painful, swollen feet in army recruits with no medical history of a specific trauma, after long periods of marching. When radiography was invented in 1895, the stress fractures were identified by doctors to occur in the metatarsals. Stress fractures often occur during prolonged exercise and are especially common in the metatarsals of military recruits, as well as runners (Meurman and Elfving, 1980; Matheson *et al.*, 1985; Giladi *et al.*, 1986; Krause and Thompson, 1944; Morris and Blickenstaff, 1967). Other clinical reports of stress fractures in athletes include ballet dancers and gymnasts who fracture the pars interarticularis (Pennel *et al.*, 1985), and golfers who fracture the hook of the hamate (Daffner, 1978). A better understanding of stress fracture etiology could help develop training regimes and therapies that would more efficiently maintain soldiers and athletes at the boundary between maximum performance and incipient fatigue failure.

1.1.2 Bone remodelling

Bone is a major and dynamic reservoir for calcium and phosphate with the processes of bone formation and resorption being tightly regulated. In the adult, bone

is constantly being remodelled to maintain an adequate supply of relatively low mineral density bone to subserve mineral homeostasis; this process involves up to 15% of the total bone mass per year (Ganong, 1981). Remodelling has also been proposed to function as a method of preventing the accumulation of fatigue damage. Although it is widely assumed that mechanical stresses influence the remodelling processes of bone (Wolff's law), neither the mathematical laws relating bone remodelling to the stress/strain environment nor the control systems which mediate these processes are understood. Proposed controlling mechanisms of bone remodelling have included micro fatigue damage, stress generated potentials, hydrostatic pressures on the extracellular fluids under load and alterations in cell membrane diffusions due to direct load (Goldstein *et al.*, 1990). The remodelling response is therefore believed to be a reparative adaptive response to fatigue damage caused by daily repeated loading.

1.1.3 Age-related spontaneous fractures

During growth phases, formation exceeds resorption and the skeletal mass increases. Equal rates of formation and resorption prevail until ages 40 to 50 years, at which time resorption begins to exceed formation and the total bone mass slowly decreases (Ganong, 1981). The rate at which bone turns over may decrease with age and this reduced rate of bone remodelling may compromise the ability to repair fatigue microcracks. If damage accumulates faster than it can be repaired, microcracks may accumulate during years of repetitive loading, compromising bone strength, and perhaps culminating in spontaneous fracture. Consequently, it is hypothesized that the fatigue behavior of bone may be a factor in the etiology of spontaneous fractures.

Approximately 10% of the 250,000 hip fractures and 50% of the 500,000 age related spine fractures that occur each year in the United States are believed to be spontaneous fractures that result not from any obvious trauma, but rather from cyclic loading of normal activity (Freeman *et al.*, 1974). Women are especially affected because they have a smaller bone mass and a more rapid rate of senescent loss than men (Ganong, 1981) with more than 40% of women 70 years of age or older experiencing one or more fractures (Christiansen, 1991). In addition to the loss of

function and associated risk of morbidity to the individual, the estimated annual medical cost for spontaneous hip and spine fractures may be over $1 billion (Keaveny and Hayes, 1993). As the elderly population increases with improved health care, the number of fractures and associated costs are expected to increase exponentially.

Thus, understanding the fatigue behavior of bone is essential from three perspectives: as the major etiologic factor in stress fractures, as a possible stimulus for bone remodelling, and as a possible etiologic factor in age-related spontaneous fractures. Additionally, since most of the components of the skeletal system are subjected to repetitive loads during normal daily activity, the fatigue properties of bone are important simply to understand the normal behavior of bone (Choi and Goldstein, 1992).

1.2 Investigating bone fatigue properties and mechanisms

The fatigue properties of bone can be investigated by using either contemporary concepts of fracture mechanics, or traditional concepts of stress and strain and applying them to cyclic loading conditions. In both approaches, the objective is to describe the strength of bone for a given number of load cycles and determining the material properties independent of the geometry. This chapter will focus on investigations using the latter approach to study the fatigue properties of the two types of bone--cortical and trabecular bone.

Cortical bone represents 80% of the total by mass and is typified by the thick shafts of the appendicular skeleton (arms and legs). Trabecular bone constitutes 20% and makes up most of the axial skeleton (vertebrae, skull, ribs) and bridges the center of the long bones (Ganong, 1981). In contrast to cortical bone, few controlled experiments have been performed on trabecular bone primarily because the heterogeneity of trabecular bone results in large data scatter, confounding the precision of analyses (Keaveny and Hayes, 1993).

1.2.1 Determining fatigue properties experimentally

In experiments where traditional engineering techniques are used to study fatigue behavior, standard specimens of bone are tested at a fixed level of stress or strain and cyclically loaded to fracture. Tests are performed at different stress levels and the fatigue life corresponding to each stress level is found. Fatigue fracture characteristically occurs at stress levels that are substantially lower than the monotonic strength.

1.2.2 Fatigue properties of cortical bone

Ever since traditional engineering techniques were first used to determine the fatigue life of compact bone specimens (Evans and Lebow, 1957), the fatigue behavior of cortical bone has been studied extensively. The parameters which have been investigated as determinants of the fatigue properties of cortical bone are loading mechanism, frequency of loading, apparent density, tissue density, temperature range, anatomic location and microstructure, stiffness, and age (Table 1.1).

Table 1.1 *Summary of the determinants of fatigue properties of cortical bone*

Parameter	**Condition that results in increased fatigue life**	**Study**
Loading Mechanism	stress reversal (vs no reversal)	Lafferty, 1978; 1979
Frequency of Loading	frequency > 30 Hz	Lafferty, 1978; 1979
Apparent Density	higher density	Gray, 1974;
Tissue Density	higher density	Carter and Hayes, 1976b; Carter *et al.*, 1976; Carter *et al.*, 1981b; Carter *et al.*, 1981a;
Temperature Range	lower temp (21°C vs 45°C)	Carter and Hayes, 1976b; Carter *et al.*, 1976;
Stiffness	higher stiffness	Carter and Hayes, 1976b; Carter and Hayes, 1977a; Keller *et al.*, 1985; Schaffler *et al.*, 1989
Age	younger age	Swanson *et al.*, 1971; Keller *et al.*, 1985

The fatigue behavior of cortical bone is much like that of composite materials. In composite materials, microscopic cracks appear as the result of repetitive loading (Jamison *et al.*, 1984). These cracks tend to run along lamellar interfaces, extending fatigue life by diverting energy from the propagation of transverse cracks which would cause more immediate failure (Kelly and Davies, 1965). In bone, similar cracks are normally present, and are differentiated from artifactual cracks by *en bloc* staining with basic fuchsin (Burr *et al.*, 1985; Mori and Burr, 1993). The number of such cracks increases following repetitive loading (Burr *et al.*, 1985; Mori and Burr, 1993). As damage accumulates through cyclic loading, there is a progressive loss of stiffness and strength (Carter and Hayes, 1977a; Carter and Hayes, 1977b; Keller *et al.*, 1985; Schaffler *et al.*, 1989; Pattin and Carter, 1990). Distinctly different types of bone microdamage are created by tensile and compressive loading. Fatigue damage created by tensile loading is characterized by separation at cement lines and interlameller

cement bands, and also by microcracking in the interstitial bone. Fatigue by compressive loading results in oblique cracking and longitudinal splitting (Carter and Hayes, 1971; Carter and Hayes, 1977b).

1.2.3 Fatigue properties of trabecular bone

The fatigue characteristics of trabecular bone are virtually unknown. Recently, fatigue experiments on individual trabeculae and cortical bone have suggested that trabecular bone tissue has a lower fatigue strength and lower moduli than cortical bone tissue (Choi and Goldstein, 1989; Ashman and Rho, 1988; Choi *et al.*, 1989, 1991; Ku *et al.*, 1987; Kuhn *et al.*, 1989; Mente and Lewis, 1989; Townsend and Rose, 1975). The difference in moduli and fatigue resistance was hypothesized to be the result of the different microstructure, mineralization, and collagen fiber orientation in the two tissues (Choi and Goldstein, 1989; Martin, 1991). Cortical bone tissue is arranged in layers of lamellae with relatively uniform mineralization. Trabecular bone is formed by surface remodelling with a higher turnover rate than cortical bone (Parfitt, 1983), thereby producing more cement lines and variable orientation. This microstructure may result in more local stress concentrators in the trabecular bone, explaining its lower fatigue resistance when compared to cortical bone.

1.2.4 Fatigue mechanisms of cortical bone

Since fatigue behavior is such an important aspect of the material properties of bone, much interest has developed in the actual mechanism of fatigue damage accumulation; however, the fatigue mechanisms are complex and still not fully understood.

A series of both experimental and theoretical studies (Carter and Caler, 1983, 1985; Caler and Carter, 1989) addressed the fatigue behavior of cortical bone. Their first study investigated the possibility that in stress-controlled cyclic tensile loading, the failure of bone is a time-dependent phenomenon in which creep-fracture may play a significant role. Stress-controlled fatigue tests in fully reversed tension-compression and in cyclic tension loading, and tensile creep-fracture tests at constant stress levels were conducted. A time-dependent failure model with a tensile loading history predicted quite well the time to failure for the cyclic tension fatigue specimens,

suggesting that creep damage plays an important role in cyclic tension fatigue specimens.

Further exploring the contribution of creep damage in fatigue loading, Carter and Caler (1985) expanded their cumulative damage model for bone fracture to account for combined creep damage and fatigue damage. The damage model predicted bone fracture from a summation of only two independent processes--creep and fatigue, where the creep-fatigue interaction was assumed to be zero. The creep and fatigue damage fractions were calculated using empirical constants derived from their previously conducted creep-fracture and fatigue-fracture experiments (Carter and Caler, 1983). The model attempted to describe the fracture behavior of bone under various loading histories and was successful in describing the influence of loading rate on monotonic tensile strength, the time to failure in constant stress creep-fracture tests, and bone fracture in zero-tension and tension-compression cyclic loading. Caler and Carter then investigated applications of the cumulative damage model previously presented and observed the nature of material damage created under various loading histories (1989). This study was the first attempt at defining some fundamental features of bone damage in cyclic and creep loading. Fatigue tests were conducted in tension, compression, and reversed loading with a tensile mean stress. Bone displayed poor creep-fracture properties in both tension and compression. The fracture surfaces of the tensile creep specimens were distinctly different than those of the compressive specimens. The study suggested that in cortical bone, creep damage dominates in the low-cycle failure regime, while fatigue damage dominates in the high-cycle regime.

1.2.5 Fatigue mechanisms of trabecular bone

Although data on the fatigue behavior of trabecular bone data are more limited than that available for cortical bone, a recent study of bovine trabecular bone demonstrated fatigue behavior similar to that of cortical bone (Michel *et al.*, 1993). Modulus degradation as a function of the number of cycles was distinctively different for high-cycle and low-cycle fatigue, suggesting differences in the response of trabecular bone to high-cycle and low-cycle fatigue. Finite element models of fatigue

and creep damage accumulation for an idealized trabecular bone specimen were developed, and the predicted number-of-cycles-to-failure were compared with the experimental data (Guo *et al.*, 1994). Predictions by the slow crack propagation model agreed well with the experimental data for the low-stress, high-cycle range, and predictions by the creep analysis model agreed well with the experimental data for the high stress, low-cycle range. These results are consistent with previous findings on cortical bone and with the hypothesis that trabecular bone fails by creep in the low-cycle fatigue regime and by microcrack damage accumulation in the high-cycle fatigue regime.

1.2.6 Improved testing methods

The data describing the fatigue behavior of trabecular bone and its comparison with that of cortical bone should be carefully interpreted, however. Researchers in the late 1980's addressed the accuracy of the experimental methods used to measure the mechanical properties of trabecular bone and identified artifacts associated with load frame compliance, and frictional and damage end effects (Linde and Hvid, 1987; Linde and Hvid, 1989; Linde *et al.*, 1992; Odgaard *et al.*, 1989; Odgaard and Linde, 1991). These experimental artifacts arise with traditional platen-to-platen compression tests in which the modulus is derived from the relative displacements between the platens. As a result, the modulus can be over- or under-estimated. To improve accuracy in mechanical testing of trabecular bone, the Orthopaedic Biomechanics Lab has developed a test protocol involving reduced-section cylindrical specimens with brass endcaps in which strain is measured directly by a miniature extensometer. This technique has been demonstrated to minimize experimental artifacts (Keaveny *et al.*, 1994). With the exception of some pilot data, the relation between fatigue loading and the number-of-cycles-to-failure has not been characterized previously using this test protocol.

An inherent assumption of the improved test protocol is that trabecular bone specimens are homogeneous in density and have a longitudinal axis which is aligned with the principal trabecular orientation. The compressive strength and stiffness of trabecular bone have been shown to be sensitive to both anisotropy (Brown and

Ferguson, 1980; Ciarelli *et al.*, 1991; Townsend, 1975) and density (Carter, 1976, 1977; Ciarelli *et al.*, 1991; Ducheynes, 1977). Thus unintentional off-axis testing can potentially introduce scatter in the experimental data and confound the interpretation of uniaxial mechanical test data. To decrease such scatter, as part of the standard technique to select specimens, contact radiographs of each cylindrical specimen are reviewed to select specimens of homogeneous density whose longitudinal axis is aligned with the principal trabecular orientation. The spatial variation of trabecular architecture within specimens harvested using this technique has not yet been quantified.

1.3 Objectives

- To validate the use of contact radiography in selecting trabecular bone specimens of homogeneous density whose longitudinal axis is aligned with the principal trabecular orientation.
- To accurately characterize the compressive fatigue behavior of devitalized bovine trabecular bone by additional mechanical testing of reduced-cylindrical specimens under loads corresponding to low stress levels normalized by the initial modulus.

1.4 Organization

The following chapter (Chapter 2) describes the use of micro-magnetic resonance imaging to validate a standard technique for selecting trabecular bone specimens. This technique is then used to select specimens for mechanical testing in Chapter 3. Chapter 3 describes these fatigue tests and presents data acquired in this study, pooled with previously reported pilot data (Guo, 1993). The pooled experimental data are then compared with predictions of two-dimensional finite element models for creep and slow crack growth in idealized trabecular bone as a first step in identifying the fatigue damage mechanism involved. The final chapter (Chapter 4) summarizes the work and includes recommendations concerning areas for further research.

Chapter 2

Using Micro-Magnetic Resonance Imaging (μMRI) to Validate a Standard Technique for Selecting Trabecular Bone Specimens

2.1 Introduction

The compressive strength and stiffness of trabecular bone have been shown to be sensitive to both anisotropy (Brown and Ferguson, 1980; Ciarelli *et al.*, 1991; Townsend, 1975) and density (Carter and Hayes, 1976, 1977; Ciarelli *et al.*, 1991; Ducheyne, 1977). A wide range of material anisotropy exists in trabecular bone, with specimens typically being either orthotropic or transversely isotropic with an isotropic plane perpendicular to the axis of symmetry. Thus, unintentional off-axis fatigue testing could introduce substantial scatter in the experimental data and cause significantly more error in some specimens than in others. Such errors due to off-axis measurements reduce the predictive power of the resulting power regression between stress (or strain) and fatigue life. An inherent assumption in uniaxial compressive fatigue tests (Chapter 3) of trabecular bone is that the axis of loading for each specimen is aligned with the principal trabecular orientation.

Initial studies of the properties of trabecular bone loaded specimens along the anatomic axes (anterior-posterior, medial-lateral, or inferior-superior) (Kuhn *et al.*, 1989; Ciarelli *et al.*, 1991) or anatomic directions (i.e. along femoral neck) (Lotz, 1990). Variability in trabecular bone moduli of as much as 100-fold have been observed from one location to another within the same metaphysis of the human proximal femur (Goldstein *et al*, 1983). Material properties of trabecular bone vary tremendously among different skeletal sites primarily because the degree of anisotropy and apparent density varies with anatomical position.

More recently, regions of homogeneous density in which the material axes are aligned with the specimen axes have been identified using contact radiography of slabs of trabecular bone from which parallelepipeds are cut. The success of this technique in aligning the material and specimen axes was investigated using surface optical stereology to measure the angle between the principal material and specimen axes (Borchers, 1991). Although optical stereology is an excellent method for quantifying the *external* morphology of trabecular bone, it is inadequate to characterize the internal trabecular architecture.

Previous investigators have noted the potential for wide variation in trabecular bone orientation throughout small specimens of bone. Variability in percent orientation of as much as 30% has been observed in an 8 mm cube of human trabecular bone (Goulet *et al.*, 1988). Thus, two-dimensional morphologic analysis may not be sufficiently accurate enough to identify specimens which are misaligned with the loading axis due to intra-specimen variations in architecture.

Three-dimensional reconstruction of the architecture of trabecular bone specimens can now be achieved with micro-magnetic resonance imaging (μMRI). Micro-magnetic resonance imaging protocols have been fully developed (Hipp and Jansjuwicz, 1993; Jansjuwicz, 1993) to produce visual reconstructions of bone specimens at a resolution comparable to what can be obtained with micro-computed tomography (Kuhn, 1990) and serial sectioning (Odgaard *et al.*, 1990). Algorithms using image processing routines such as thresholding functions and fourier transforms, and bone morphology routines such as the method of directed secants have also been developed and validated (Hipp and Jansjuwicz, 1993; Jansjuwicz, 1993) to calculate mean intercept lengths, anisotropy, volume fraction, and the principal orientations together with the three-dimensional reconstructions.

Currently, as part of the standard technique for selecting specimens (described below) a set of contact radiographs of each cylindrical specimen is reviewed to select specimens of homogeneous density whose longitudinal axis is aligned with the principal trabecular orientation. The spatial variation of trabecular architecture within specimens harvested using this technique has not yet been quantified. Because off-

axis testing confounds the interpretation of uniaxial mechanical test data, the longitudinal specimen axis must be aligned with the principal trabecular orientation during fatigue tests. **Thus the aim of this study was to validate the use of contact radiography in selecting trabecular bone specimens of homogeneous density whose longitudinal axis is aligned with the principal trabecular orientation.** To characterize the principal material axes over the entire *volume,* three-dimensional micro-magnetic resonance images were obtained. Using methods based on directed secants, alignment of the longitudinal axis with the principal trabecular orientation and degree of anisotropy were determined. Additionally, area fraction of solid in serial slices through a typical specimen was determined to investigate the homogeneity of density.

2.2 Materials and methods

2.2.1 Standard technique for selecting specimens for mechanical testing

Cylindrical cores of bovine trabecular bone were harvested from fresh proximal tibia following the Orthopaedic Biomechanics Laboratory's standard procedure for preparation of bovine trabecular bone specimens (Figs. 2.1- 2.3). After the fresh bone was procured from a local slaughterhouse (Bertolino Beef Co., South Boston, MA, USA), the soft tissue and fascia were removed from the tibia, and the head of the proximal tibia was separated from the diaphysis using a band saw (1 HP #C.92 H, Food Machinery of America, Buffalo, NY, USA). The proximal head was then cut sagittally into 12 mm thick slabs (Fig. 2.1a). Contact radiographs (Kodak X-OMAT TL Diagnostic Film #158 3293, Eastman Kodak, Rochester, NY, USA) of these slabs were taken (Faxitron Model #43855A A04, Hewlett-Packard, McMinnville, OR, USA) and used to identify regions of trabecular bone of homogeneous density and anisotropy (Fig. 2.1b). From these identified homogeneous regions, 40 mm x 12 mm x 12 mm rectangular prisms were traced using a template and then cut with the band saw, ensuring that the principal orientation of the trabeculae within the central 5 mm gage length was aligned with the prism axes (Fig. 2.2a). Using a diamond-tipped coring

(a)

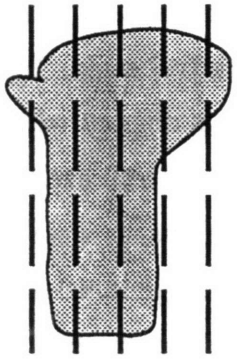

(b)

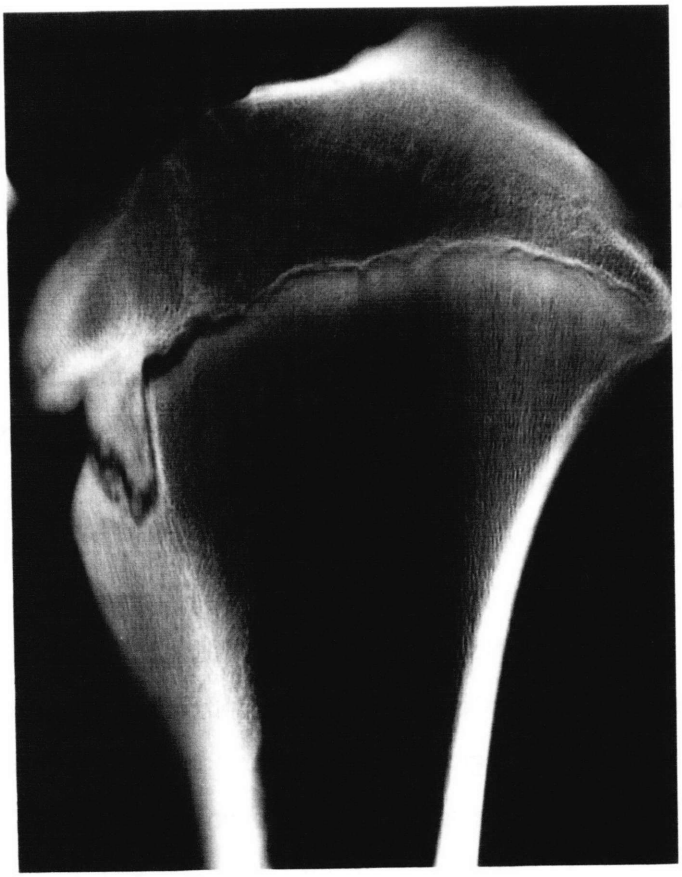

Figure 2.1: (a) Head of the proximal tibia cut sagittally into slabs. From Keaveny et al. (1994).
(b) Contact radiograph of a typical slab used to identify homogeneous regions.

tool (Starlite, Rosemont, PA, USA) one bone cylinder (diameter, d = 8.3 mm) was cored from each of these prisms (Fig. 2.2b).

Contact radiographs of the cylinders were independently reviewed by three investigators with regard to three criteria: orientation, density, and length. Acceptable specimen cores were required to have 1) a strong axis of orientation, with the principal orientation of the trabeculae being aligned longitudinally with the core axis (Fig. 2.2c); 2) uniform trabeculae density in the central 5 mm gage length region where failure would occur (Fig. 2.3a); 3) a length greater than 35 mm to accommodate the brass end caps (to be added in the next stage), the central 5 mm waisted gage length region, and 3 - 4 mm of bone between the waisted length and the end caps (Fig. 2.3b). Only specimens meeting all three requirements advanced to the final stages of specimen preparation for mechanical testing (Fig. 2.3c).

2.2.2 Specimen Preparation for Micro-Magnetic Resonance Imaging (μMRI)

Because the specimen selection and preparation method is rather labor-intensive, this study was coordinated with an unrelated study so that a single set of specimens was used in both studies. One of the objectives of the other study was to quantify modulus errors in the traditional compression test (Keaveny *et al.*, 1995). In that study, specimens were loaded in compression for ten cycles under strain control at +/- 0.4% and then for ten cycles under displacement control at 0.06 mm. These applied loads are well below the threshold for altering any of the structural properties of trabecular bone, permitting the use of these specimens in this study.

After mechanical testing, the bone within the gage length was machined from the specimen with a low speed saw (Isomet, Buehler Corp., Lake Bluff, IL, USA) equipped with a diamond wafering blade operating under copious irrigation (Fig. 2.4a). The resulting specimen had a 1:1 aspect ratio with height and diameter measuring 6 mm (Fig. 2.4b). The specimens were prepared for micro-magnetic resonance imaging following standard lab procedure (OBL SOP #IA_M_1, Version #2) (Hipp and Jansjuwicz, 1993; Jansjuwicz, 1993). The marrow space contents were removed from the bone specimens by ultrasonic agitation (Fisher Ultrasonic Cleaning System, Fisher Scientific, Pittsburgh, PA, USA) with a 1:3 bleach:water solution. After 15 - 20

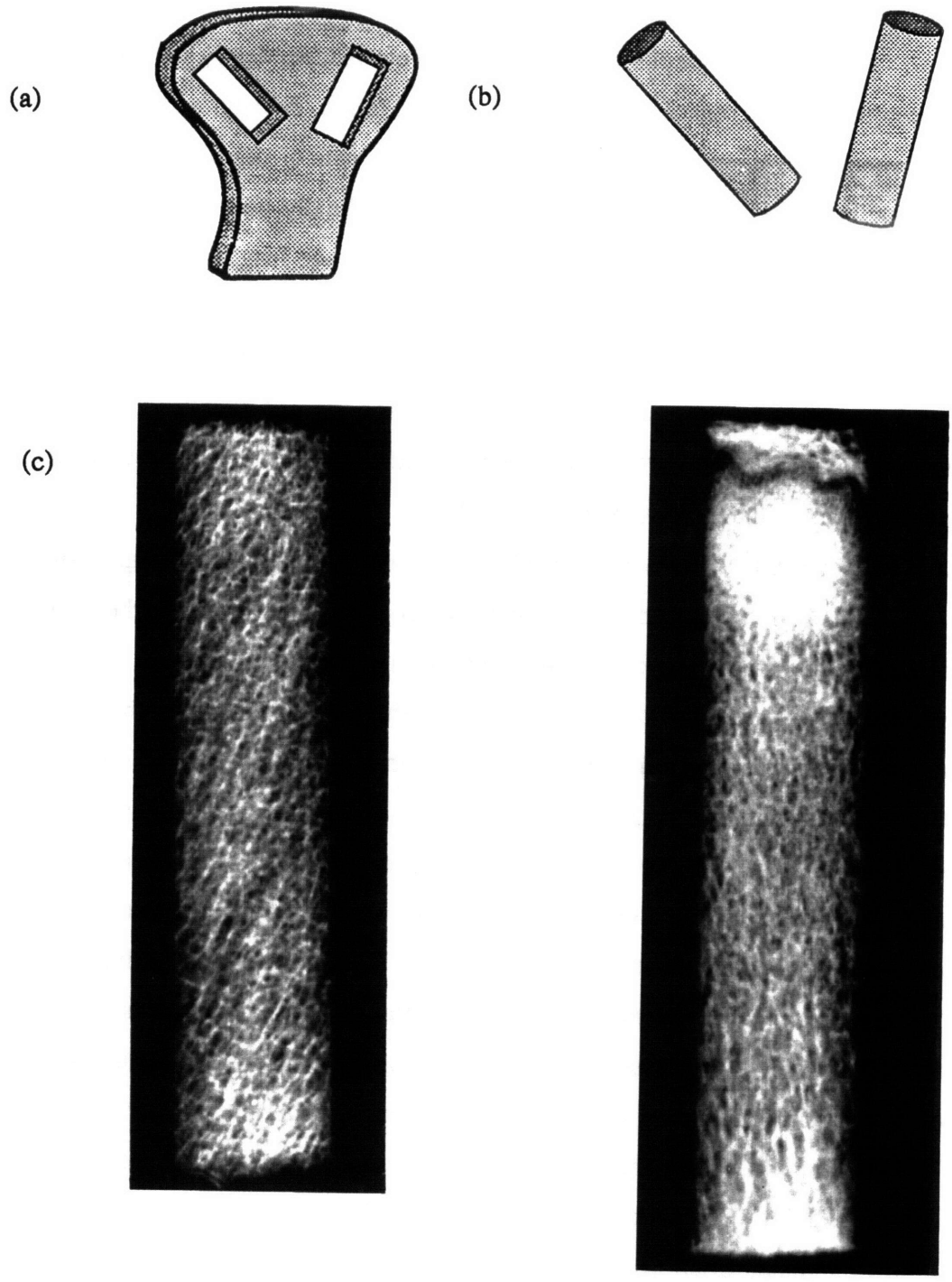

Figure 2.2: (a) Rectangular prisms cut from identified homogeneous regions. From Keaveny et al. (1994). (b) One bone cylinder cored from each rectangular prism. From Keaveny et al. (1994). (c) Contact radiographs of typical rejected specimen cores whose longitudinal axis is not aligned with the principal trabecular orientation (left) or do not have a strong axis of orientation (right).

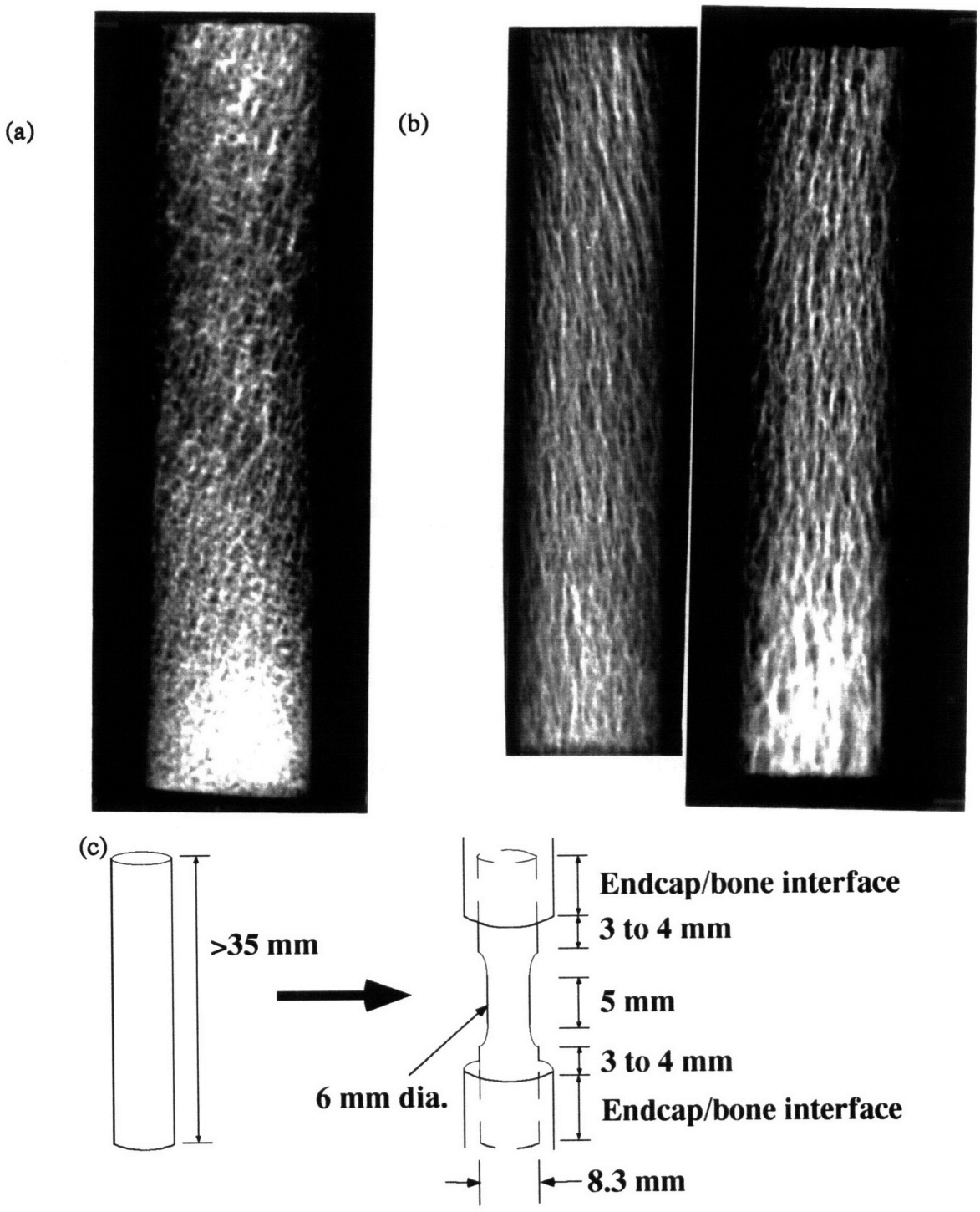

Figure 2.3: (a) Contact radiograph of a typical rejected specimen core that does not have uniform trabeculae density in the central 5 mm gage length region. (b) Examples of acceptable specimen cores (c) Acceptable cores must have a length greater than 35 mm.

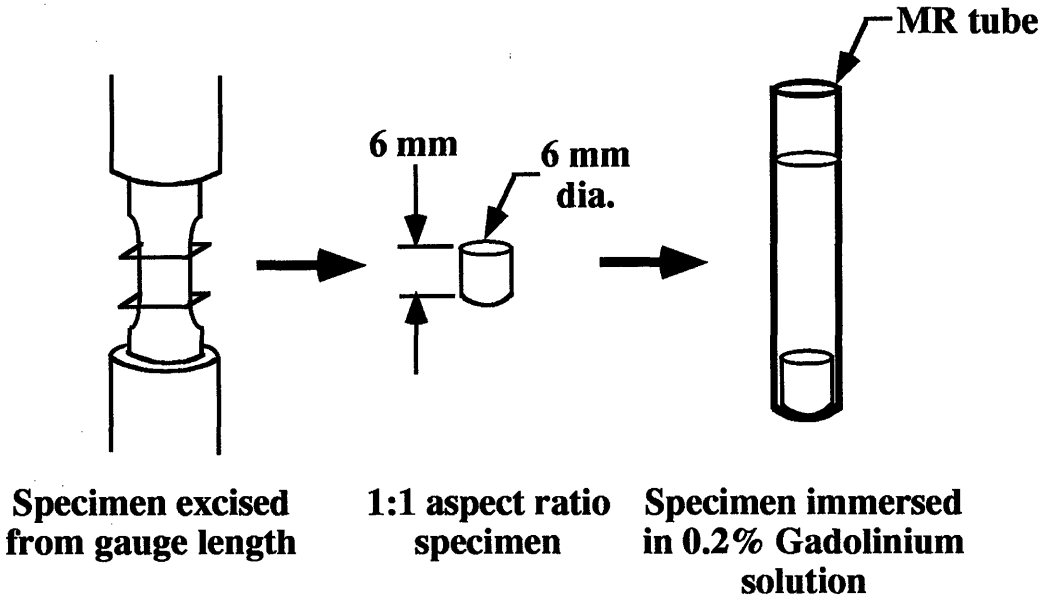

Figure 2.4: Specimen preparation for micro-magnetic resonance imaging following standard lab procedure. (a) The bone within the gage length was machined from the specimen. (b) The resulting specimen had a height = 6 mm, diameter = 6mm. (c) Specimens were immersed in magnetic resonance contrast medium.

minutes of agitation, the cloudy solution was replaced with fresh bleach solution. Ultrasound was continued and the process repeated until the dilute bleach solution remained clear but for no longer than a total of 45 minutes.

The specimens were then placed in magnetic resonance compatible tubes and immersed in magnetic resonance contrast medium of 0.2 mg/ml solution of gadopentetate dimegumine per 100 ml of distilled water (Fig. 2.4c). Replacing the marrow phase with the gadopentetate solution provided a more homogeneous imaging medium. The immersed specimens were degassed under vacuum to remove any trapped air bubbles that would otherwise appear as areas of low signal intensity in the image and would be incorrectly identified as bone. Specimens remained under vacuum until the bubbling rate of the specimens was negligible.

2.2.3 Micro-Magnetic Resonance Imaging

The degassed, immersed specimens were imaged following standard lab procedure (OBL SOP #IA_M_1,Version #2) (Hipp and Jansjuwicz, 1993; Jansjuwicz, 1993) using a Bruker AM spectrometer (Bruker Instruments, Inc., Billerica, MA) with micro-imaging accessory and a 10 mm H^1 radio frequency coil. The field of view was set to 7.841 mm in all directions and the raw data stored to a 128 x 128 x 128 array. The resolution obtained using these parameters was 61.3 microns along each edge of the voxels. An algorithm with low and high thresholds was used to classify each voxel in the variance image as being either bone or marrow space (Hipp and Jansjuwicz, 1993; Jansjuwicz, 1993). The binary three-dimensional image files were viewed using Sunvision (SUN Microsystems, Mountain View, CA, USA) and AVS-based custom software (Application Visual System (AVS), Advanced Visual Systems Inc., Waltham, MA, USA).

2.2.4 Analysis of Micro-Magnetic Resonance Images

Material symmetry and orientation angle Each reconstructed three-dimensional image was automatically centered and a 5000 micron (5.0 mm) diameter spherical region of interest was chosen. Methods based on directed secants were used to analyze this constant volume of bone (Snyder, 1991; Hipp and Jansjuwicz, 1993; Jansjuwicz, 1993). The three-dimensional mean intercept length (MIL) vector was

determined for each of 128 randomly oriented rotations of a three-dimensional collinear test line array at a parallel testline spacing of 200 microns. The MIL vector was a statistical estimate of the average length between phase boundaries within one phase and was defined as:

$$MIL = \frac{\textit{total length of test lines} * \textit{bone vol fraction}}{\frac{1}{2} * \textit{no. of intersections between test lines and phase boundaries}} \quad (2.1)$$

An ellipsoid was fit to the MIL vectors and the properties of the ellipsoid were used to describe anisotropic properties of the bone sample The angle between the longitudinal axis of the specimen and the principal trabecular orientation was determined by solving the equation and orientation of the ellipsoid with respect to the principal axes and was defined as the angle between the projection of the MIL vector on the x-y plane and the maximum principal MIL vector. The degree of material anisotropy in one principal direction i was defined as:

$$\textit{degree of anisotropy} = \frac{\textit{prin value in dir. i - mean prin value of all 3 dir.}}{\textit{mean principal value}} \quad (2.2)$$

where the principal values were the lengths of the individual ellipsoid semi-axis lengths. The mean trabecular thickness was also determined for each image; it was given by:

$$\textit{mean trabecular thickness} = \frac{2 * \textit{bone vol. fraction}}{\textit{boundary interface length betwn bone \& marrow}} \quad (2.3)$$

Homogeneity. The variability in homogeneity through a specimen was investigated in a typical specimen. Using the post-processing software (Application Visual System (AVS), Advanced Visual Systems Inc., Waltham, MA, USA), the reconstructed image could be sectioned in any plane to visualize the internal structure of the specimen. Five serial slices parallel to the longitudinal axis of the specimen were imaged using a high resolution monochrome videocamera (CCD 72 Series Camera, Dage-MTI, Inc., Michigan City, IN, USA) equipped with a 50 mm lens

(Olympus Corp., Japan) and a video digitizing system (SUN Videopix board, SUN Microsystems, Mountain View, CA, USA). Each digitized image was 640 by 480 pixels, resulting in a resolution of 20 microns per pixel. An algorithm based on iterative edge detection was used to automatically determine a grey-level threshold delineating bone and marrow spaces (Snyder *et al.*, 1990; Hipp and Jansjuwicz, 1993; Jansjuwicz, 1993). The two-dimensional mean intercept length vectors of a circular test region were determined for each of 64 evenly spaced rotations of a two-dimensional collinear test line array at a testline spacing of 200 microns. The two-dimensional MIL vector was also defined by Eqn. (2.1), with bone area fraction substitute for the bone volume fraction. An ellipse was fit to the MIL vectors and the orientation of the major principal material axis was estimated from the ellipse fit to these data. The area fraction of the solid was determined through a pixel counting routine within the circular test region:

$$area\ fraction = \frac{number\ of\ pixels\ representing\ bone}{total\ number\ of\ pixels} \qquad (2.4)$$

2.2.5 Criteria for determining acceptable range of specimen alignment

A Hankinson-type relationship and Tsai-Hill formula were used to determine an acceptable degree of misalignment of the angle between the longitudinal axis of the specimen and the principal trabecular orientation that still ensures accuracy in the strength measurements.

Hankinson formula. The original Hankinson relationship was formulated for determining the compressive strength of wood (Hankinson, 1921) and has been adapted to successfully predict the off-axis strength of human cortical bone (Reilly and Burstein, 1975), but not yet applied to trabecular bone. The Hankinson-type formula relates the off-axis ultimate compressive strength of a trabecular bone specimen to the ultimate strengths in the two principal directions, and is given by:

$$s(\Phi) = \frac{s(90)\,s(0)}{s(90)\cos^n(\Phi) + s(0)\sin^n(\Phi)} \qquad (2.5)$$

where Φ = angle between the longitudinal axis of the specimen and the principal trabecular orientation (orientation angle)

$s(\Phi)$ = off-axis ultimate compressive strength at angle Φ

$s(0)$ = ultimate longitudinal compressive strength i.e. strength of a trabecular bone specimen in which the longitudinal axis of the specimen is perfectly aligned with the principal trabecular orientation ($\Phi = 0°$)

$s(90)$ = ultimate transverse compressive strength i.e. strength of a trabecular bone specimen in which the longitudinal axis of the specimen is perpendicular to the principal trabecular orientation ($\Phi = 90°$)

n = experimentally derived parameter

The ultimate compressive strength of a specimen as determined by the Hankinson formula (Eqn. 2.5) can be expressed as a fraction of the ultimate longitudinal compressive strength; we define relative strength S_H as determined by the Hankinson formula:

$$\textit{relative strength} = S_H = \frac{\textit{off-axis ultimate strength}}{\textit{ultimate longitudinal compressive strength}} = \frac{s(\Phi)}{s(0)} \qquad (2.6)$$

The relative strength S_H as determined by the Hankinson-type relationship is dependent upon the strength anisotropy ratio and an empirically determined constant n. We define strength anisotropy ratio R as:

$$\textit{strength anisotopy ratio} = R = \frac{\textit{ultimate longitudinal compressive strength}}{\textit{ultimate transverse compressive strength}} = \frac{s(0)}{s(90)} \qquad (2.7)$$

The strength anisotropy ratio for the ultimate compressive strength of trabecular bone specimens is 2.9 (Pinilla *et al.*, 1993); here, we take a value of 3. The constant, n, has not been empirically determined for trabecular bone. We assumed a value of n = 2.0 for trabecular bone as determined for wood (Forest Products Laboratory, 1990) and cortical bone when tested in compression (Reilly and Burstein, 1975). Using a strength anisotropy ratio of 3 and assuming n = 2.0 in the Hankinson-type relationship (Eqn. 2.6), the relative strength of a trabecular bone specimen S_H was plotted against orientation angle Φ.

Tsai-Hill formula. The Tsai-Hill formula predicts failure strengths in off-axis uniaxial tensile tests and is based on the von Mises failure criterion which was originally applied to homogeneous and isotropic bodies (Hull, 1981). The criterion was later expanded and modified to anisotropic bodies and applied to successfully predict the variation of strength with angle for composite materials such as carbon fiber-epoxy resin laminae. The Tsai-Hill formula accounts for the interactions between the tensile stresses which lead to transverse tensile cracks and the shear stresses which lead to intralaminar cracks on the same fracture plane. The criterion can be used to predict the failure strength in off-axis tests on unidirectional laminae and may be expressed as:

$$S(\Theta) = \left[\frac{\cos^4\Theta}{s(0)^2} + \left(\frac{1}{s(\tau)^2} - \frac{1}{s(0)^2}\right)\sin^2\Theta\cos^2\Theta + \frac{\sin^4\Theta}{s(90)^2}\right]^{-\frac{1}{2}} \qquad (2.8)$$

where Θ = angle between the longitudinal axis of the specimen and the principal trabecular orientation (orientation angle)

$s(\Theta)$ = off-axis ultimate strength at angle Θ

$s(0)$ = ultimate longitudinal strength i.e. strength of a trabecular bone specimen in which the longitudinal axis of the specimen is perfectly aligned with the principal trabecular orientation ($\Theta = 0°$)

$s(90)$ = ultimate transverse strength i.e. strength of a trabecular bone specimen in which the longitudinal axis of the specimen is perpendicular to the principal trabecular orientation ($\Theta = 90°$)

$s(\tau)$ = ultimate shear strength

The ultimate strength of a specimen as determined by the Tsai-Hill criterion (Eqn. 2.8) can be expressed as a fraction of the ultimate longitudinal strength; we define relative strength S_T as determined by the Tsai-Hill criterion:

$$relative\ strength = S_T = \frac{off\text{-}axis\ ultimate\ strength}{ultimate\ longitudinal\ strength} = \frac{s(\Theta)}{s(0)} \quad (2.9)$$

Recently available longitudinal and transverse ultimate tensile and compressive strength and shear strength data for bovine trabecular bone specimens (Pinilla *et al.*, 1993; Ford and Keaveny, 1995) were used to plot the relative strength S_T of a specimen against orientation angle Θ for four different cases of loading and mean apparent density. Ultimate tensile and compressive failure data for specimens with mean apparent densities of approximately 0.65 g/cc, and ultimate shear data for specimens with mean apparent densities of 0.55 g/cc and 0.65 g/cc were plotted.

Table 2.1: *Ultimate failure data for Tsai-Hill criterion*

Case	s(0) (MPa) loading cond. mean app. dens. (g/cc)	s(90) (MPa) loading cond. mean app. dens. (g/cc)	s(τ) (MPa) loading cond. mean app. dens. (g/cc)
I	16.9 **Tensile** 0.61	5.85 **Tensile** 0.69	10.56 Longitudinal **0.55**
II	16.9 **Tensile** 0.61	5.85 **Tensile** 0.69	12.5 Longitudinal **0.65**
III	23.6 **Compressive** 0.62	8.13 **Compressive** 0.72	10.56 Longitudinal **0.55**
IV	23.6 **Compressive** 0.62	8.13 **Compressive** 0.72	12.5 Longitudinal **0.65**

(Pinilla *et al.*, 1993; Ford and Keaveny, 1995)

Acceptable degree of misalignment using Hankinson and Tsai-Hill. For a specimen in which the longitudinal axis of the specimen is perfectly aligned with the principal trabecular orientation, the relative strength is 1.0. Specimens having a compressive strength greater or equal to 0.85 of the longitudinal ultimate compressive strength s(0) were considered to have acceptable alignment. From the plot of the Hankinson formula applied to trabecular bone, the maximum acceptable degree of misalignment of the angle between the longitudinal axis of the specimen and the principal trabecular orientation Φ_{max} corresponding to $s(\Phi)/s(0) = 0.85$ was determined. Similarly, from the plot of the Tsai-Hill formula applied to trabecular bone, the maximum acceptable degree of misalignment of the angle between the longitudinal axis of the specimen and the principal trabecular orientation Θ_{max} corresponding to $s(\Theta)/s(0) = 0.85$ was determined.

2.3 Results

2.3.1 Maximum acceptable degree of misalignment

Hankinson formula. Using a strength anisotropy ratio of 3 and assuming $n = 2$ for trabecular bone in the Hankinson-type relationship (Eqn. 2.6), the relative strength S_H of a trabecular bone specimen was plotted against orientation angle (Fig. 2.5). From Fig. 2.6, we found $\Phi_{max} = \pm 17°$, where Φ_{max} is the maximum acceptable degree of misalignment of the angle between the longitudinal axis of the specimen and the principal trabecular orientation corresponding to $S_H = s(\Phi)/s(0) = 0.85$.

Tsai-Hill formula. Using available ultimate failure strength data (Table 2.1) in the Tsai-Hill criterion (Eqns. 2.8 and 2.9), the relative strength S_T of a trabecular bone specimen was plotted against orientation angle for four cases (Fig. 2.7). From Fig. 2.8, we found $22° < |\Theta_{max}| < 33°$, where Θ_{max} is the maximum acceptable degree of misalignment of the angle between the longitudinal axis of the specimen and the principal trabecular orientation corresponding to $S_T = s(\Theta)/s(0) = 0.85$. The lower bound of the range of acceptable orientation angles ($\Theta_{max} = 22°$) resulted from Case III test conditions (Table 2.1). Case III used $s(\tau)$ for specimens with a mean apparent

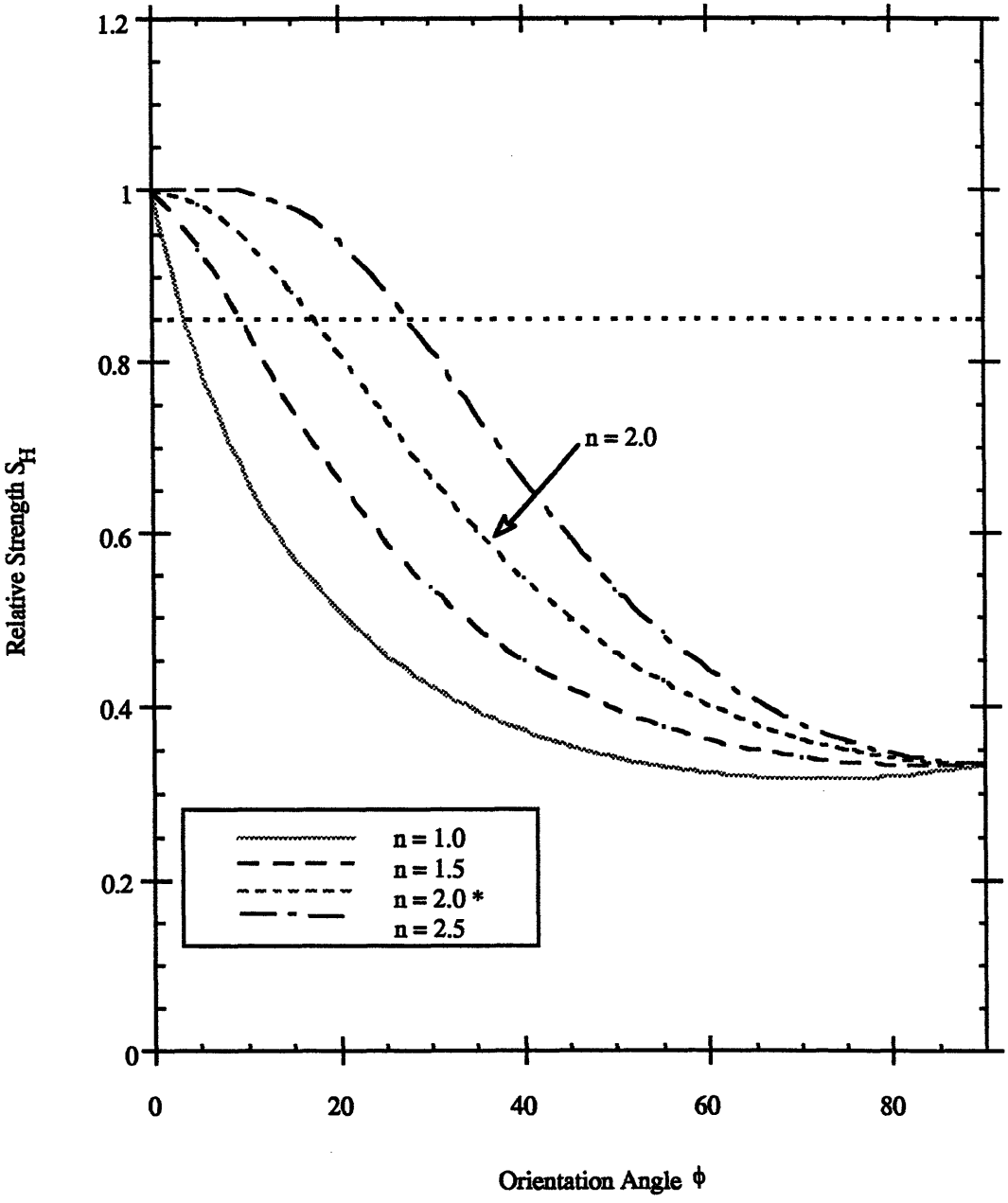

Figure 2.5: Hankinson formula applied to trabecular bone with strength anisotropy ratio = 3 and experimentally derived parameter n= 1.0, 1.5, 2.0, 2.5.

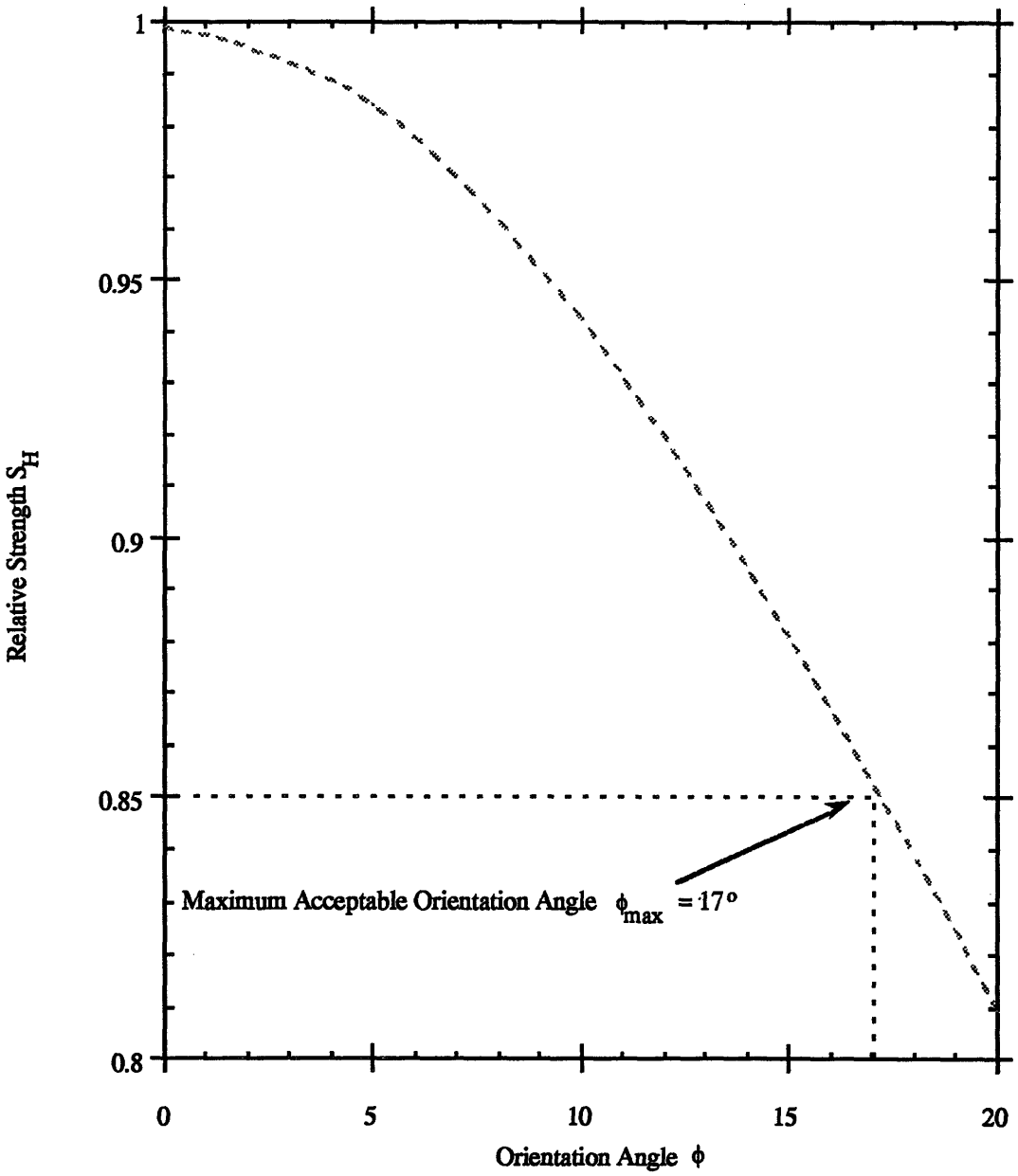

Figure 2.6: Maximum acceptable orientation angle corresponding to relative strength = 0.85 as determined by Hankinson formula (strength anisotropy ratio = 3, n = 2).

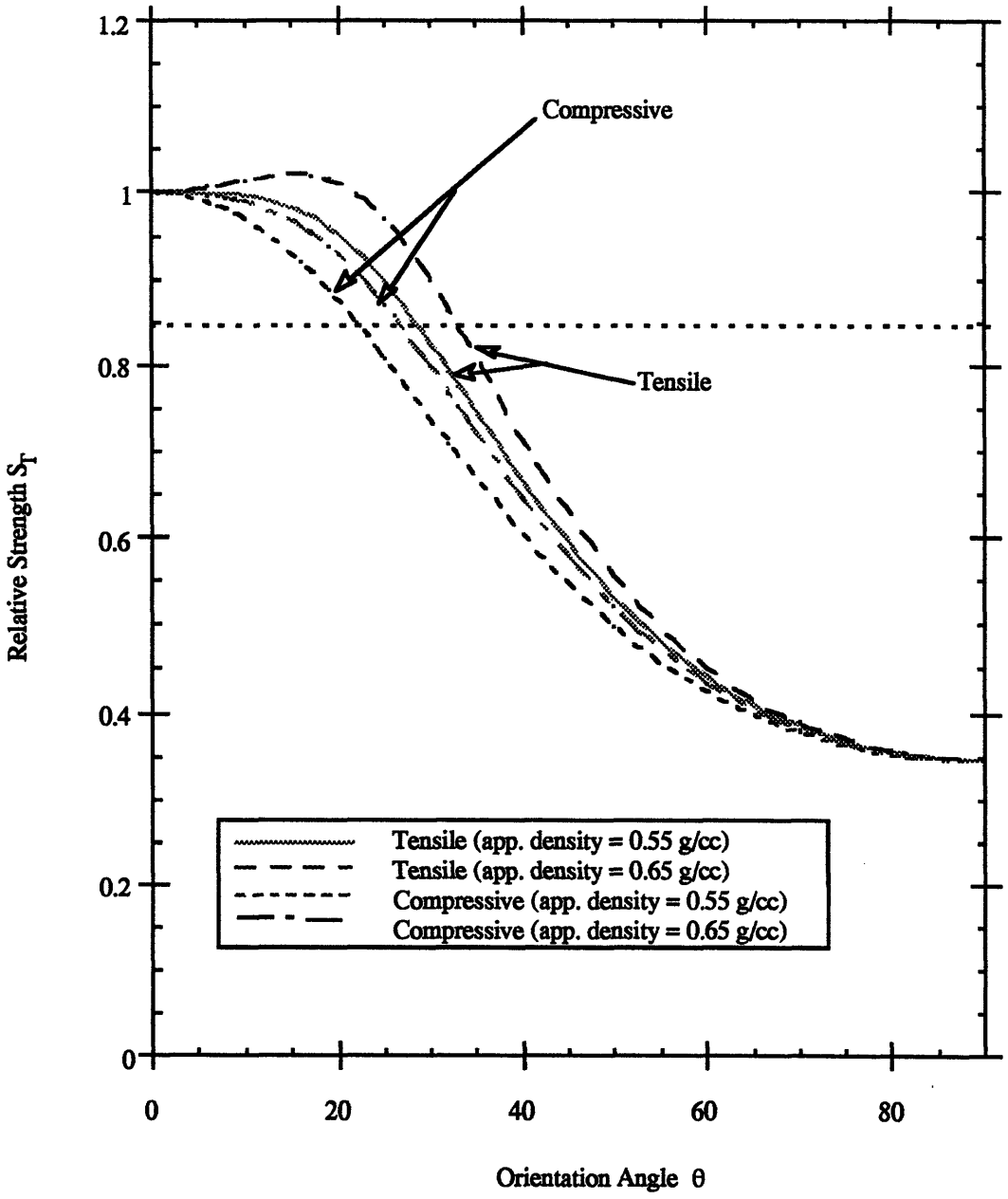

Figure 2.7: Tsai-Hill formula applied to trabecular bone using s(0) and s(90) values for specimens with apparent densities = 0.65 g/cc under tension and compression, and s(τ) for specimens with apparent densities = 0.55, 0.65 g/cc.

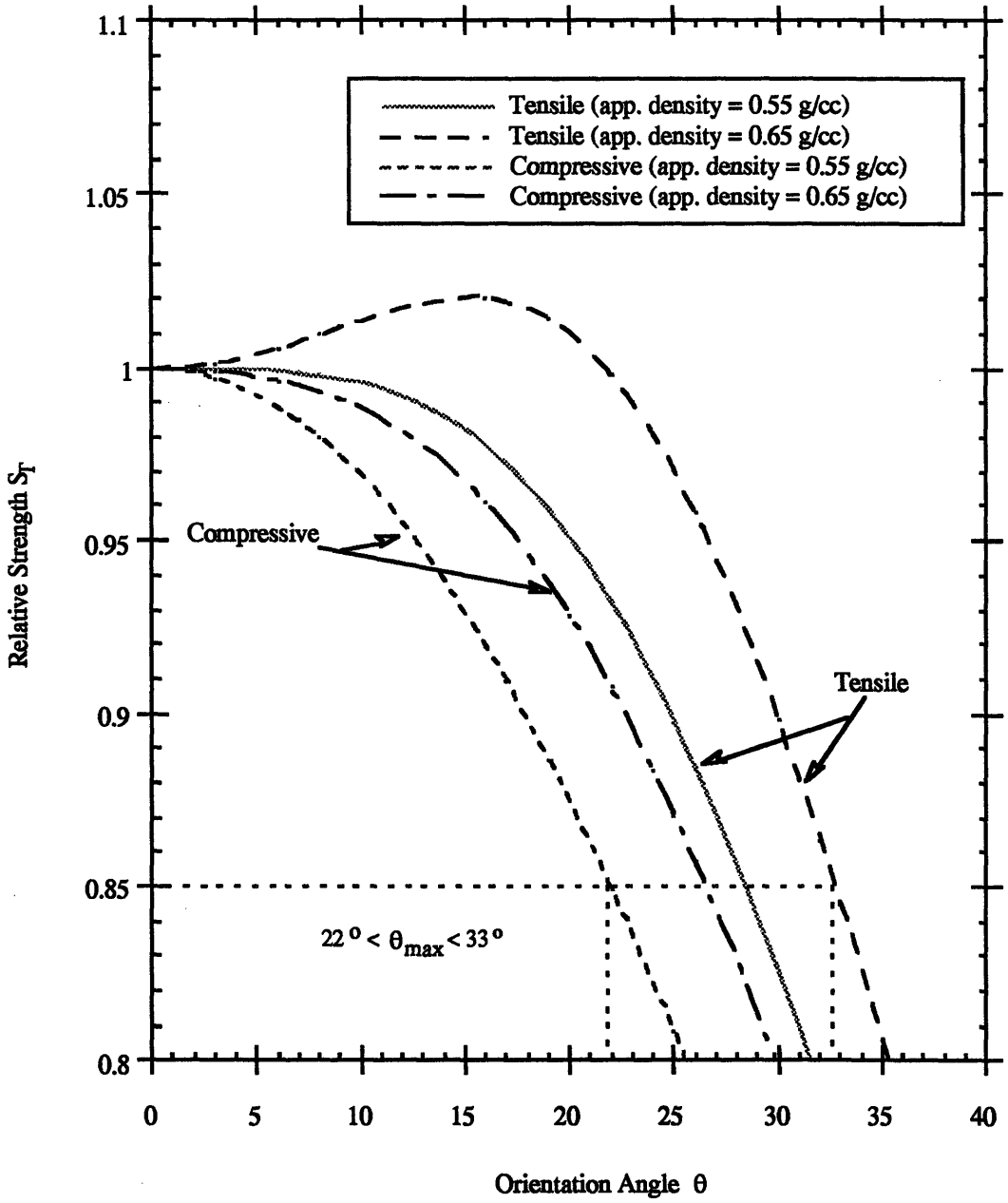

Figure 2.8: Range of maximum acceptable orientation angles corresponding to relative strength = 0.85 as determined by the Tsai-Hill formula.

density = 0.55 g/cc, and s(0) and s(90) of specimens loaded in compression. The upper bound of the range of acceptable orientation angles (Θ_{max} = 33°) resulted from Case II test conditions (Table 2.1). Case II used the s(τ) of specimens with a mean apparent density = 0.65 g/cc, and s(0) and s(90) of specimens loaded in tension.

2.3.2 Material symmetry and orientation angle

One three-dimensional micro magnetic resonance image was obtained for each of twelve bovine trabecular bone specimens. Images were repeated for two of the specimens, resulting in 14 total images (Fig. 2.9). The orientation angle ranged from 2.13° - 20.63° (Fig. 2.10), with the relative strength S_H as determined by the Hankinson formula ranging from 0.81 - 1.0 (Fig. 2.11) and the relative strength S_T as determined by the Tsai-Hill criterion ranging from 0.87 - 1.0 (Fig. 2.12). Twelve of the 14 images had an acceptable degree of misalignment as determined by the Hankinson formula (orientation angle $\Phi < 17°$), and all 14 of the images had an acceptable degree of misalignment as determined by the Tsai-Hill formula (orientation angle $\Theta < 22°$). Four of the fourteen images were classified as transversely isotropic and ten as orthotropic. The mean trabecular thickness ranged from 0.26 - 0.52 mm.

2.3.3 Homogeneity

The variation in homogeneity through the depth of a specimen was investigated for a typical specimen (Fig. 2.13). Analysis of five serial slices parallel to the longitudinal axis for the specimen estimated the mean area fraction of the solid was 0.36 (SD 0.035), the mean ratio of major to minor mean intercept lengths was 1.31 (SD 0.14), and the mean orientation of the major principal material axis was 3.2° (SD 3.8°).

2.4 Discussion

Although previous investigators have observed a wide variation in orientation over small regions of trabecular bone, our micro-magnetic resonance imaging results indicate that our current selection technique using contact radiographs ensures an acceptable degree of misalignment between the principal trabecular orientation and the

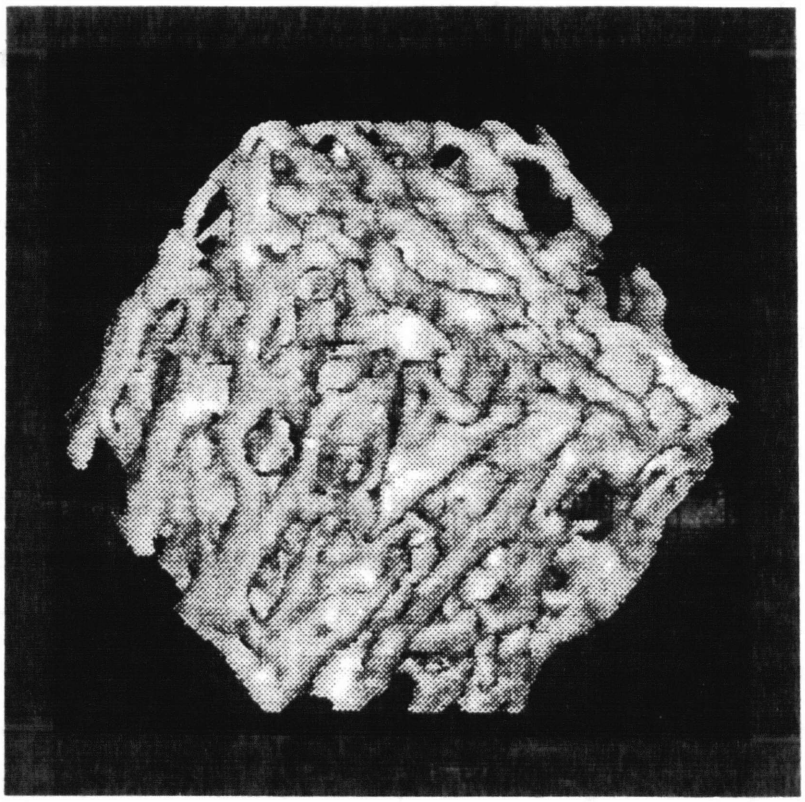

Figure 2.9: Reconstructed three-dimensional image of typical trabecular bone specimen. From Jansjuwicz (1993).

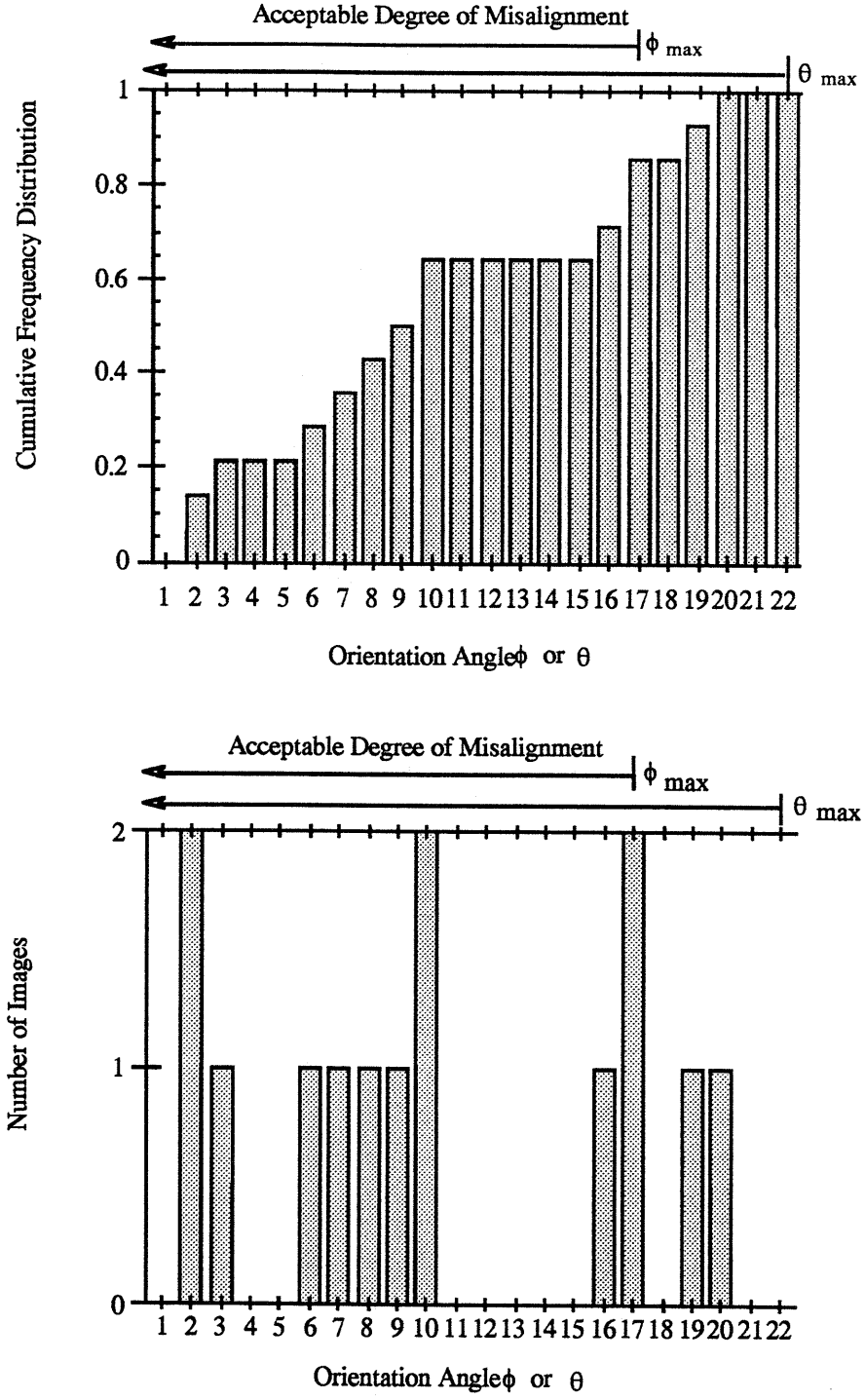

Figure 2.10: Cumulative frequency distribution of the orientation angle of specimen images (top) and number of images for given orientation angles (bottom). 0.86 of the total number of images had an orientation angle $\Phi < \Phi_{max}$ where $\Phi_{max} = 17^{o}$ as determined by the Hankinson criterion. All of the images had an orientation angle $\Theta < \Theta_{max}$ where $\Theta_{max} = 22^{o}$ as determined by the Tsai-Hill criterion.

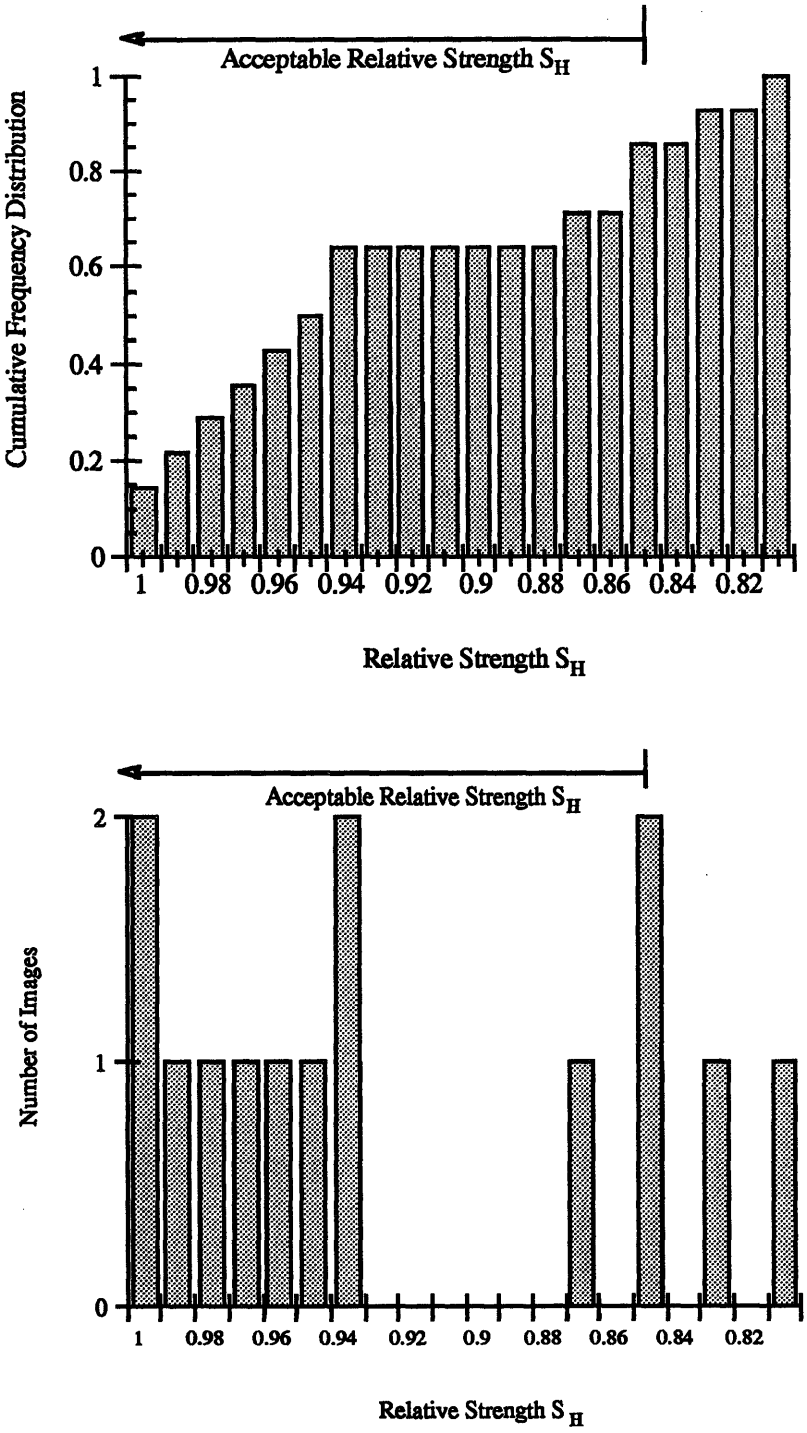

Figure 2.11: Cumulative frequency distribution of the relative strength of images (top) and number of images for a given relative strength (bottom) as determined by the Hankinson criterion. 0.86 of the total number of images had a relative strength > 0.85.

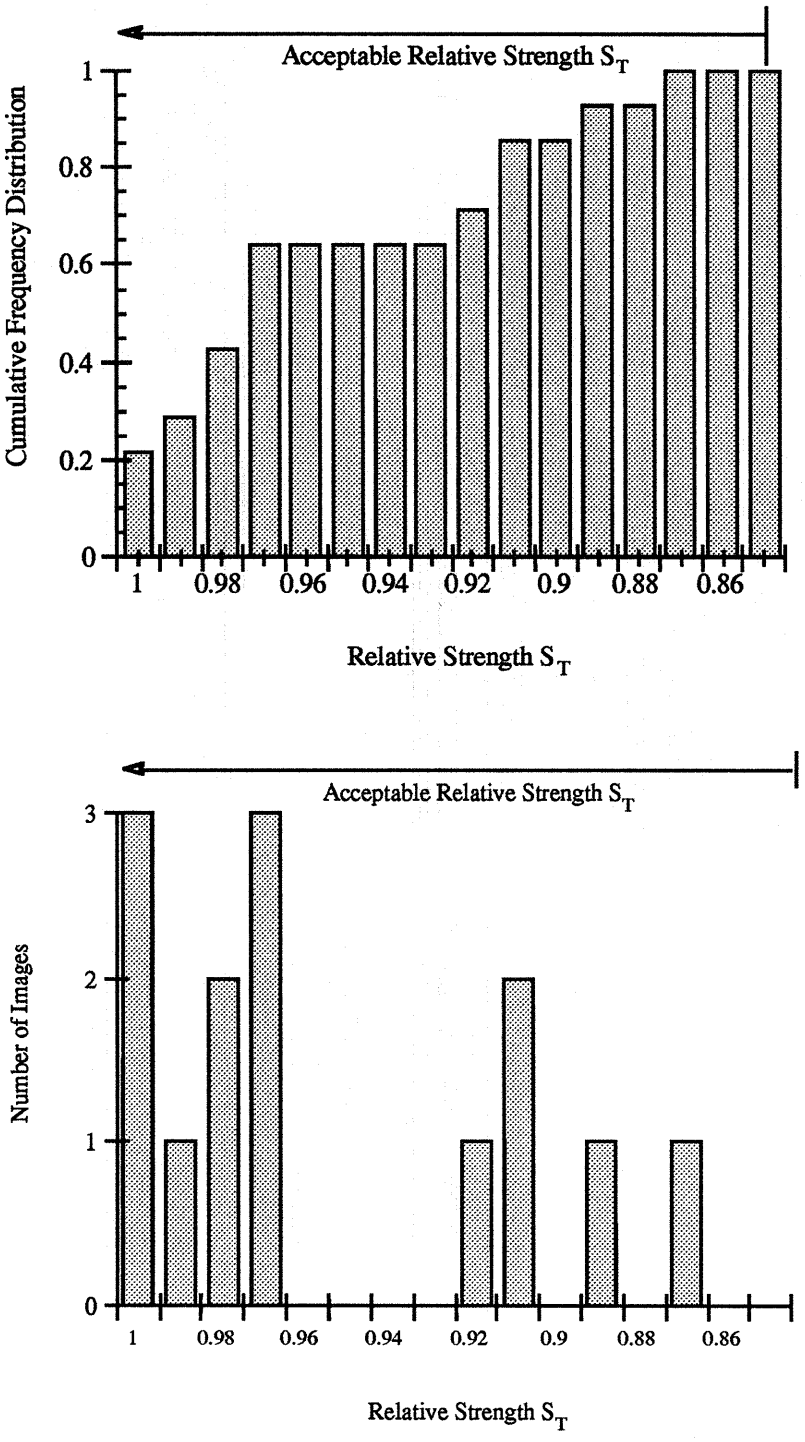

Figure 2.12: Cumulative frequency distribution of the relative strength of images (top) and number of images for a given relative strength (bottom) as determined by the Tsai-Hill criterion. All of the total number of images had a relative strength > 0.85.

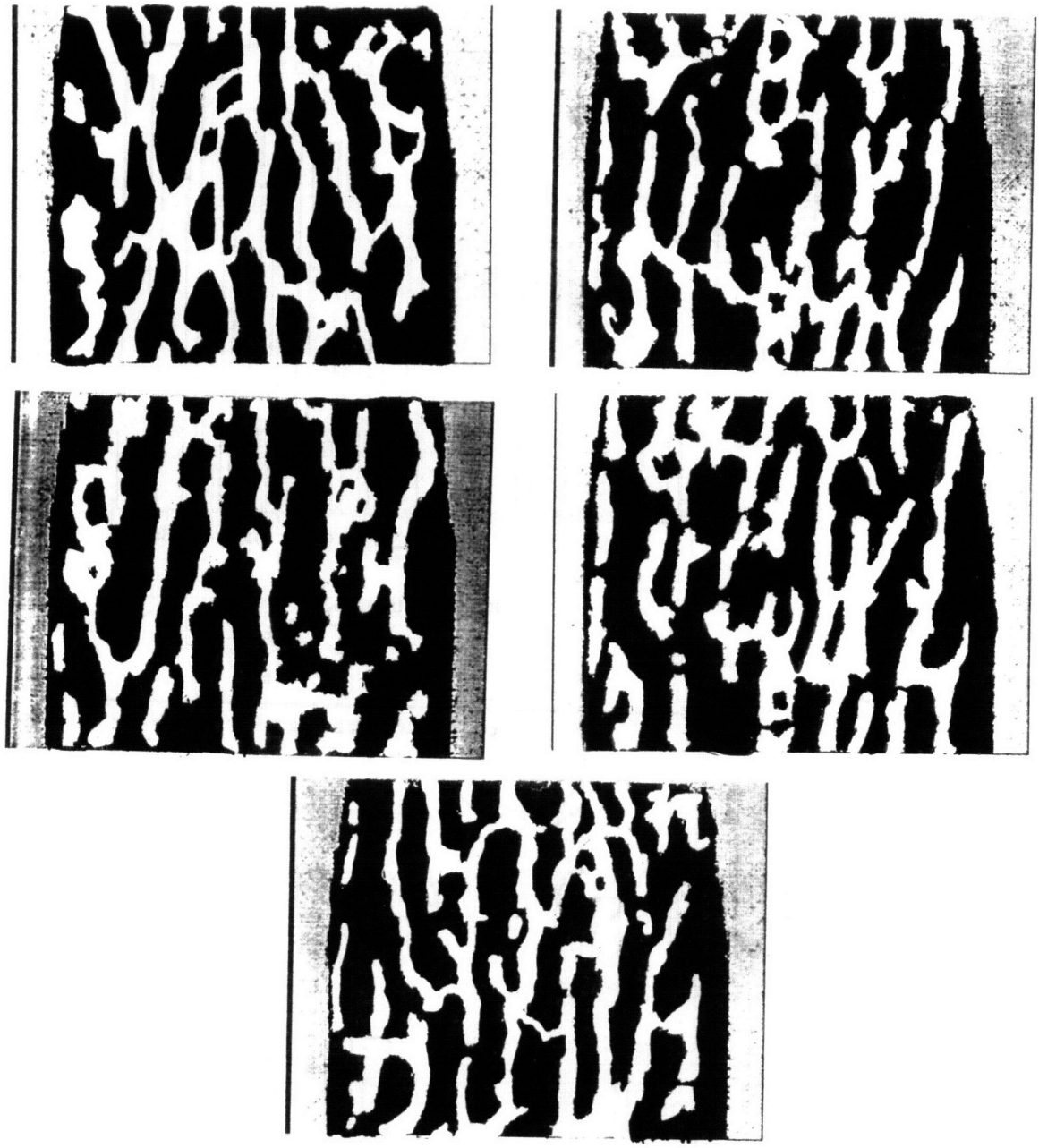

Figure 2.13: Micro-MRI images of parallel two-dimensional slices from a typical specimen of trabecular bone showing homogeneity throughout the specimen.

longitudinal axis of the specimen. Twelve of the 14 images had an acceptable degree of misalignment as determined by the more conservative Hankinson criterion (orientation angle $\Phi < 17°$), and all 14 of the images had an acceptable degree of misalignment as determined by the Tsai-Hill formula (orientation angle $\Theta < 22°$). The low coefficient of variation of the area fraction (CV 0.09) of the serial slices throughout a typical specimen indicated that we were also successfully screening the specimens for homogeneity of density based on contact radiographs. Thus we are adequately controlling the alignment and density of specimens to an acceptable level.

2.4.1 Strengths of this study

Recently acquired data on the ultimate strengths (shear, longitudinal and transverse compressive) of bovine trabecular bone specimens (Pinilla *et al.*, 1993; Ford 1995) enabled us to apply the Hankinson and Tsai-Hill criteria to determine an acceptable degree of misalignment. Previously reported data on the failure properties of bovine trabecular bone may be inaccurate due to limitations in mechanical testing methods. The mechanical testing protocol employed in these recent studies, however, allowed for accurate measurements of the ultimate strengths by directly measuring the strain in the reduced section of the cylindrical specimen which is biased to failure to reduce experimental artifact. Additionally, the trabecular bovine specimens were selected using the same standard specimen selection technique as in this MRI study.

Unlike stereology measurements of the surfaces of trabecular bone, which do not explain the variation that exists internal to these surfaces, well-developed micro-magnetic resonance procedures enabled us to reconstruct images showing the *internal* structure of trabecular bone and quantify the three-dimensional architecture of trabecular bone.

2.4.2 Limitations

A complete multi-axial failure criterion that also accounts for variations in trabecular bone density may be the best criterion to determine the off-axis strength of the trabecular bone specimens. To date, a complete multi-axial failure criterion such as the Tsai-Wu criterion has not been formulated for trabecular bone to account for variations in trabecular bone density and architecture. However, the ultimate failure

strengths s(0), s(90), and $s(\tau)$ for trabecular bone are known, enabling us to apply a Hankinson-type relationship and Tsai-Hill formula. Although the Hankinson and Tsai-Hill criteria were not formulated for trabecular bone but for wood and unidirectional laminae, respectively, the morphology of wood and unidirectional laminae are similar to that of trabecular bone (Gibson and Ashby, 1988). The Hankinson criterion was originally formulated for use in timber framing to determine the compressive strength of wood on surfaces at an angle to the grain and has been adapted in a similar manner to successfully predict the off-axis strength of human cortical bone using on-axis data (Reilly and Burstein, 1975). Therefore the Hankinson and Tsai-Hill formulas may not be unreasonable alternatives to a complete multi-axial failure criterion for determining an acceptable degree of misalignment in trabecular bone.

A linear regression of the ultimate failure strength of bovine trabecular bone as a function of apparent density was available for $s(\tau)$; however, s(0) and s(90) values were available only for specimens with a mean apparent density approximately = 0.65 g/cc. Using the linear regression of $s(\tau)$ as a function of apparent density, the $s(\tau)$ for trabecular bone with an apparent density = 0.65 was calculated and used in Cases II and IV. The specimens fatigued in the compression tests (Chapter 3) had a mean apparent density = 0.55 g/cc. The $s(\tau)$ for trabecular bone with an apparent density = 0.55 was calculated and used in Cases I and III. Without a linear regression of s(0) and s(90) as a function of apparent density, the ultimate failure strength values did not correspond to exactly the same apparent density within a case. This may be one possible explanation for the maximum relative strength of Case II unexpectedly occurring at an orientation angle $\Theta = 15$ and not $\Theta = 0$.

A linear regression of the ultimate failure strengths of bovine trabecular bone as a function of apparent density has not been determined for s(0) and s(90).

Although the Tsai-Hill criterion was formulated and has been employed to successfully predict the failure strength in off-axis uniaxial **tensile** tests only, we applied the Tsai-Hill criterion to predict both tensile and compressive failure strengths. Applying compressive s(0) and s(90) values (Case III) to the Tsai-Hill criterion resulted in the lower bound of Θ_{max}. Although the lower bound value of Θ_{max} and

Φ_{max} were approximately equal ($\Theta_{max} \approx \Phi_{max} \approx 17°$), the results of Case III and IV which applied the Tsai-Hill failure criterion to predict **compressive** failure strengths must be carefully interpreted.

The experimentally derived parameter n in the Hankinson formula which is related to the degree of anisotropy has not been determined for trabecular bone and was assumed to equal that determined for wood and estimated for cortical bone. The parameter n = 2.0 was derived for wood (Forest Products Laboratory, 1990), a cellular solid with a degree of anisotropy similar to trabecular bone (Gibson and Ashby, 1988). Additionally, when a value of n = 2.0 was used in the Hankinson-type relationship to predict failure loads for cortical bone, the predictions agreed well with experimental values. Although cortical and trabecular bone have different porosities and architecture, cortical bone is usually considered transversely isotropic (Reilly and Burstein, 1975; Yoon and Katz, 1976) and the tissue properties of cortical bone and trabecular bone are believed to be similar (Carter and Hayes, 1977). Therefore, an assumption of n = 2.0 for trabecular bone may not be unreasonable.

The algorithm to determine the degree of anisotropy had not been fine-tuned at the time the images were analyzed. The results of this study indicate that the trabecular bone specimens were more likely to be orthotropic than transversely orthotropic. The new thresholding algorithm may be overly sensitive to orthotropy. The anisotropy results for Images 13 and 14 support this possibility. Although the two images are of the same specimen and the orientation angles agree well with each other (69° and 73°), Image 13 was determined to be orthotropic and Image 14 was determined to be transversely isotropic. The program is currently being modified to address this possibility.

2.4.3 Comparison with previous study

Previously, specimens were selected based on contact radiography of slabs of trabecular bone. Stereological analysis on the faces of parallelepipeds from which the cylindrical specimens are cored indicated that the maximum degree of anisotropy ranged from 2.4% to 46.3% and the ratio of the maximum to the minimum principal mean intercept lengths varied up to a value of roughly 2.21 for all faces measured. As

a result, uniaxial compressive strengths can vary by a factor of up to 9.7 within a specimen as determined from uniaxial tests conducted in each of the three principal directions of the specimen reference frame (Borchers, 1991). An additional set of contact radiographs of the cylindrical specimens has since been added to the standard specimen selection technique. The orientation angle between the longitudinal axis of the specimen and principal trabecular orientation ranged from 2.13° - 20.63°, with the relative strength ranging from 0.81 - 1.0 based on Eqn. (2.6). These results suggest that we are now adequately controlling the alignment of the specimens.

2.4.4 Future directions

The assumption that the constant n = 2 for trabecular bone in the Hankinson-type relationship should be validated. Compression tests similar to those performed on cortical bone (Reilly and Burstein, 1975) could be conducted on longitudinal, radial and intermediate angle trabecular specimens to determine the off-axis ultimate strength and the constant n for trabecular bone.

To apply a multi-axial failure criterion such as the Tsai-Wu failure criterion, one must determine experimentally up to 12 independent coefficients depending on the material anisotropy. Additional uniaxial and multi-axial experiments to determine the unknown coefficients in the mathematical form of the criterion could be conducted to formulate the criterion. The heterogeneous and porous nature of trabecular bone creates an added complexity to performing the mechanical tests. Calculations can then be repeated using the multi-axial failure criterion to more accurately determine an acceptable degree of misalignment.

Recent progress in micro-magnetic resonance imaging at our laboratory now enables scanning of the specimens with the marrow in place. This flexibility adds to the robust power of micro-magnetic resonance imaging as a tool for future projects.

2.5 Conclusions

In conclusion, the use of contact radiography in selecting specimens indeed yields homogeneous specimens whose longitudinal axes are aligned with the principal

trabecular orientations. New micro-magnetic resonance imaging techniques enabled us to validate our specimen selection technique using three-dimensional reconstructions and characterizations of the architecture of the bone specimens, and not two-dimensional stereology measurements of the surfaces which cannot explain internal variations that may exist. Therefore, using our specimen selection technique, we are able to ensure that the alignment and density of specimens are of an acceptable level so that this technique may be employed when selecting specimens for future uniaxial mechanical tests.

Chapter 3

Compressive High Cycle Fatigue Behavior of Bovine Trabecular Bone

3.1 Introduction

Approximately 10% of the 250,000 hip fractures and 50% of the 500,000 age related spine fractures that occur each year in the United States are believed to be spontaneous fractures that result from the cyclic loading of normal activity (Freeman *et al.*, 1974). These fatigue fractures are commonly found in the trabecular components of the proximal femur, vertebrae, calcaneus and tibia. Thus an understanding of the fatigue behavior of trabecular bone is essential for estimating the risk of these spontaneous fractures. In addition, microdamage caused by bone fatigue under physiologic cyclic loading has been hypothesized to be a major stimulus for bone remodelling (Pugh *et al.*, 1973b; Burr *et al.*, 1985).

The *in vitro* fatigue behavior of cortical bone has been studied extensively. Creep and fatigue damage fractions of a damage accumulation model for human cortical bone fracture have been calculated using empirical relations derived from creep-fracture and fatigue-fracture experiments (Caler and Carter, 1989; Carter and Caler, 1983, 1985). This model successfully described strain rate effects on monotonic tensile strength, time to failure in tensile creep-fracture tests, and fracture in cyclic loading. The study suggested that in cortical bone creep damage dominates in the low-cycle failure regime, while fatigue damage dominates in the high-cycle regime.

Although data on fatigue behavior of trabecular bone are limited, a recent study of bovine trabecular bone demonstrated fatigue behavior similar to that of cortical bone (Michel *et al.*, 1993). Modulus degradation with the number of cycles was distinctively different for high-cycle and low-cycle fatigue, suggesting differences in the response of trabecular bone to high-cycle and low-cycle fatigue

(Keaveny and Hayes, 1993; Michel *et al.*, 1993). Finite element models of fatigue and creep damage accumulation for an idealized trabecular bone specimen were developed, and the predicted number-of-cycles-to-failure were compared with the experimental data (Guo *et al.*, 1994). There was no significant difference between the slope of the stress range versus the number-of-cycles-to-failure curve (S-N) predicted by the slow crack propagation model and the experimental data for the low-stress, high-cycle range. Likewise, the slope of the S-N curve predicted by the creep analysis model and that of the experimental data agreed well for the high-stress, low-cycle range. These findings further support the hypotheses that the primary mechanism for low-stress, high-cycle fatigue of trabecular bone is crack growth and propagation, while the primary failure mechanism for high-stress, low-cycle fatigue is creep deformation and fracture.

The data describing the fatigue behavior of trabecular bone should be carefully interpreted, however. The fatigue study of cubic specimens employed a traditional compression testing protocol of trabecular bone in which machined specimens are loaded between two rigid platens, and the modulus is calculated from the relative displacements of the platens. A slight initial increase in modulus in the high-cycle, low-stress regime of the cubic specimens was believed to be an artifact associated with a compliant layer of trabeculae at the ends of the specimen due to machining (Michel *et al.*, 1993). The identification of other artifacts associated with load frame compliance, frictional and damage end effects that arise with the traditional trabecular bone compression test (Linde and Hvid, 1987; Linde and Hvid, 1989; Linde *et al.*, 1992; Odgaard *et al.*, 1989; Odgaard and Linde, 1991) has prompted the development of improved testing protocols (Ashman *et al.*, 1987; Ashman *et al.*, 1989; Bensusan *et al.*, 1983; Kaplan *et al.*, 1985; Keaveny *et al.*, 1994). A pilot fatigue study using an improved testing protocol involving reduced-section cylindrical specimens in which strain is measured directly with a miniature extensometer investigated whether the initial increase in modulus observed in the fatigue of cubic specimens was an experimental artifact (Guo, 1993). Results using

this technique suggested that this new protocol minimizes experimental artifacts (Keaveny *et al.*, 1994).

The relation between fatigue loading and the number-of-cycles-to-failure for trabecular bone specimens has not been characterized previously using this improved testing protocol. The pilot fatigue study investigating experimental artifacts provided preliminary data to characterize this relationship (Guo, 1993). **Thus, this study is aimed at accurately characterizing the compressive fatigue behavior of devitalized bovine trabecular bone by additional mechanical testing of reduced-section cylindrical specimens under loads corresponding to low stress levels normalized by the initial modulus.** This study is a continuation of the pilot fatigue study and is designed so that acquired data can be pooled with the previously reported pilot data (Guo, 1993). The change in normalized Young's modulus with the number of cycles of loading will be measured and used to characterize damage. Additionally, experimental data will be compared with predictions of two-dimensional finite element models for creep and slow crack growth in idealized trabecular bone as a first step in identifying the fatigue damage mechanism involved.

3.2 Materials and Methods

3.2.1 Specimen Preparation for Mechanical Testing

Cylindrical cores of bovine trabecular bone were harvested from fresh proximal tibia following the Orthopaedic Biomechanics Laboratory's standard procedure for preparation of bovine trabecular bone specimens as described in **Section 2.2.1 Standard technique for selecting specimens for mechanical testing.**

Quantitative computed tomography (QCT) of the selected specimens was conducted at Somerset Technologies, Boston, MA,USA, and the Radiology Division of Beth Israel Hospital, Boston, MA, USA (Fig. 3.1a). The QCT values were analyzed with AVS-based (Advanced Visualization Systems, Waltham, MA, USA) custom software to calculate the density of the specimens.

From the final batch of acceptable bone cores, 32 specimens were randomly

selected and prepared for mechanical testing. In order to create a suitable bone surface on which to mount the end caps, the specimen ends were defatted with a high-pressure water jet. Each specimen end was then dipped in 100% ethanol for one minute and dried in an air jet. The inside of each end cap was coated with two drops of cyanoacrylate glue (Prism, 401, Loctite, Newington, CT, USA). To ensure axial alignment of the specimen in the brass end caps, first the end caps were positioned in a custom-fit jig and then the bone was press-fit into the end caps (Fig. 3.1b, c). Care was taken to ensure that the central gage length remained hydrated and free from ethanol and adhesive during the end-capping process.

The end-capped specimens were then protected with plastic wrap and frozen in dry ice in -70° C for approximately 3 hours. Immediately after being removed from dry ice, the specimen was turned down on a lathe with a 1/4 inch radius cutting tool to form the waisted geometry (6 mm diameter, 10 mm long gage length) (Fig. 3.1d) with minimal microdamage (Fig. 3.2). During the entire specimen preparation process, precautions were taken to minimize improper handling or storing of the bone tissue which would affect the bone's material properties. To prevent the bone tissue from dehydrating, the specimens were either wrapped in wet gauze or soaked in a cool (21° C) water bath during all stages of the specimen preparation. The specimens were always stored in wet gauze wrap and placed in sealed bags or containers at -20° C. Prior to any handling, these wrapped specimens were thoroughly thawed either at room temperature or in a cool (21° C) water bath. Since each freeze/thaw cycle also affects a bone's material properties, the number of freeze/thaw cycles was minimized. A total of 32 bovine specimens were prepared, each from a different proximal tibia.

3.2.2 Fatigue Tests

The fatigue tests were conducted in a servohydraulic material test machine (Instron Model 1331, Instron Corp., Canton, MA, USA) equipped with a 500 lb Instron load cell. Prior to each fatigue test, the alignment of the Instron load frame was measured with an alignment transducer held in the 3-jaw chucks. The transducer had the same dimensions as the non-waisted compound bone/endcap specimen and was equipped with two strain gages equally spaced around the transducer's

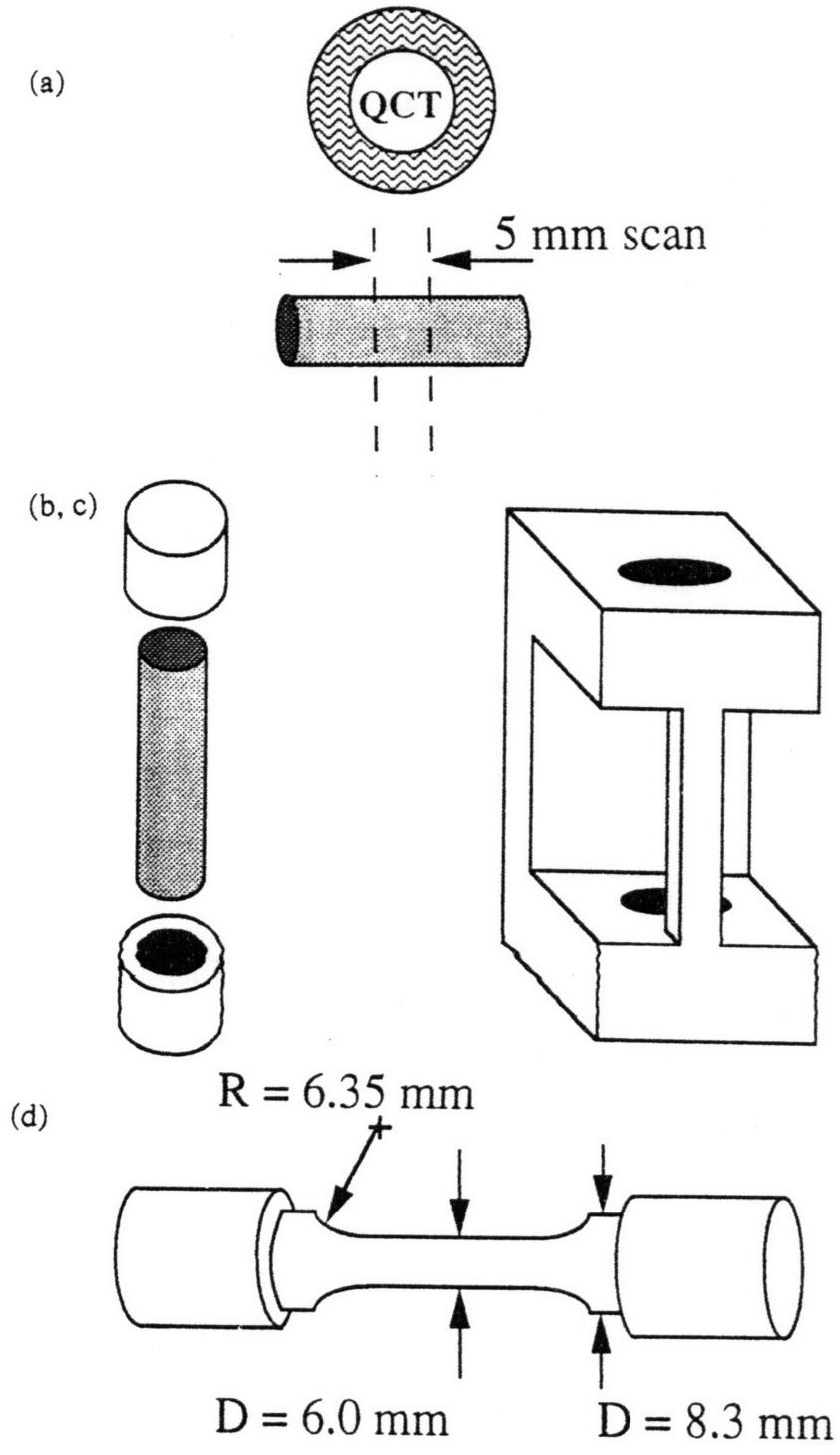

Figure 3.1: (a) QCT of selected specimens.
(b, c) Bone press-fit into end caps using a custom-fit jig to position the bone
(d) Specimen turned down on a lathe to form
waisted geometry. From Keaveny et al. (1994).

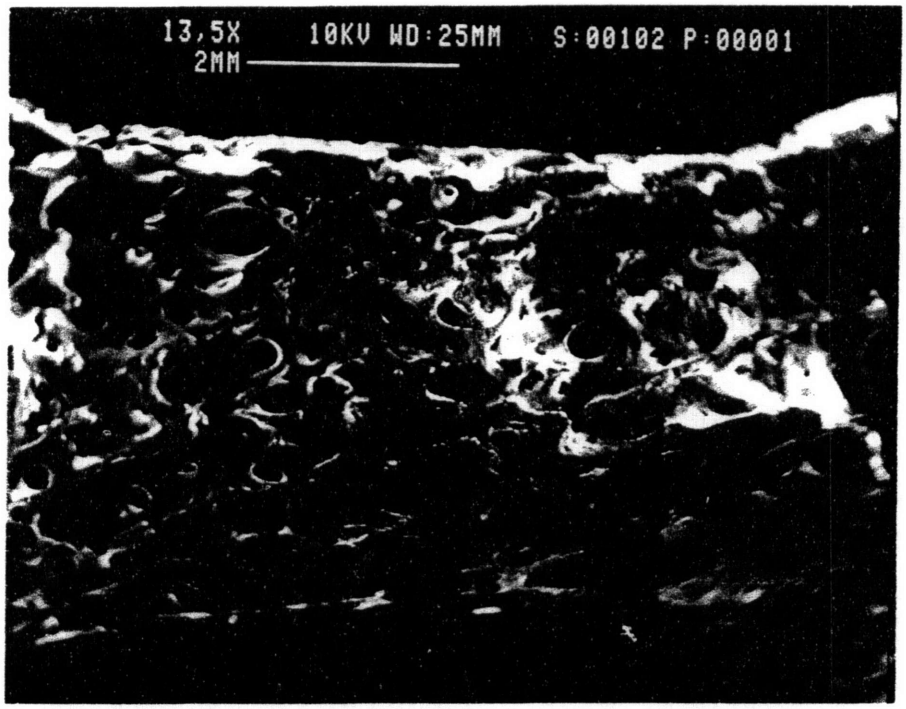

Figure 3.2: Scanning electron micrograph of prepared specimen with minimal microdamage.

circumference to measure bending. Strain levels were measured each time the transducer was rotated 120° within the 3-jaw chucks (Fig. 3.3). The Instron load frame was adjusted until bending was minimal (strain level < 200 microstrains) and the frame was adequately aligned for three consecutive rotations.

The diameters of each specimen were measured six times with a digital electronic caliper (Model 500-351, Mitutoyo Corp., Japan) before mechanical testing, with the resulting mean values used for all subsequent calculations. A miniature 16 g, 5 mm gage length extensometer (MTS, MN, Model #632-29C-30) mounted directly on the waisted portion of the specimen measured the deformation and a constant 0.9% physiological saline solution drip hydrated the specimen throughout the test. Pre-conditioning and fatigue tests were conducted at room temperature under a cyclic compressive sinusoidal load profile at 2 Hz. Specimens were pre-conditioned for 10 cycles under strain control from 0% strain (defined at 10 N compressive load) to 0.2% compressive strain. Pre-conditioning data was recorded using a personal computer (Dell Computers Model 316, Austin, TX, USA) and Labtech Notebook (Laboratory Technologies, Corp., Wilmington, MA, USA). The initial strain range was converted to a stress range, and the test load level corresponding to the desired test strain level was then extrapolated from this linear pre-conditioning stress-strain relationship (Fig. 3.4). Specimens were fatigued under load control from 10 N (compressive defined at 0% strain) to this calculated test load at a load frequency of 2 Hz. Load and strain data from the fatigue tests were acquired with an Interlaken Universal Test Program III (UTP III) (Interlaken Technology Corp., Eden Prairie, MN, USA). To optimize computer memory, data for the number-of-cycles-to-failure was acquired at a logarithmic rate. For each cycle, 200 data points were sampled at 0.0025 seconds sample time between points. The range of the channels were +/- 1100 N for the load channel, +/- 5 mm for the stroke channel and +/- 5% for the strain channel. Fatigue failure was defined as either 10% decrease in initial secant modulus (E_o) or fracture (exceeding the limit on strain channel of 5%). The number-of-cycles-to-fracture was read from the monitor and recorded in the lab notebook designated for the study. 31 of the 32 prepared specimens were fatigued to various

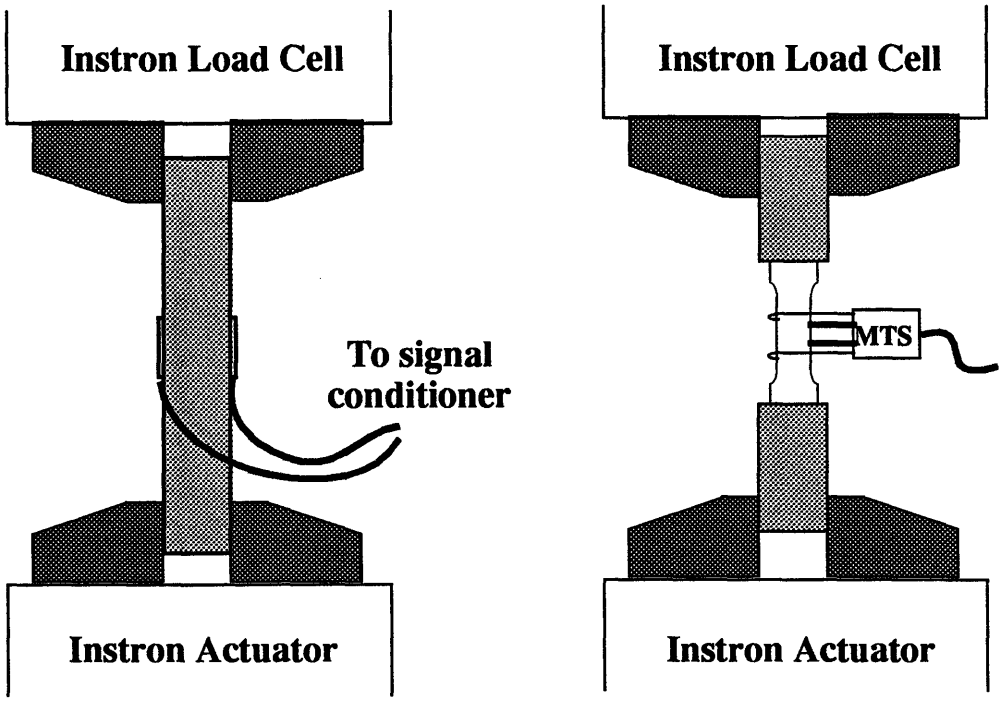

Figure 3.3: Alignment of Instron load frame with alignment transducer (left) and testing of prepared trabecular bone specimen with miniature extensometer (right).

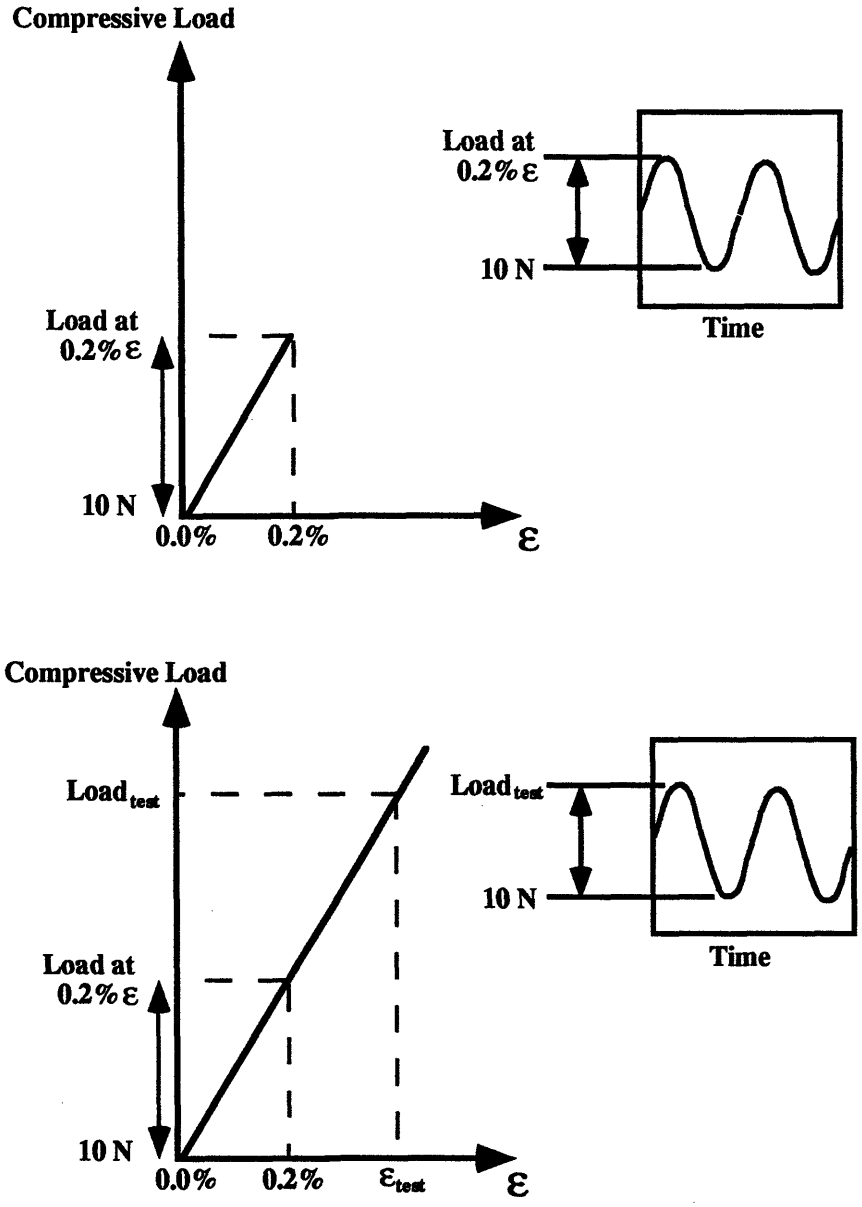

Figure 3.4: Preconditioning for 10 cycles under strain control from 0% to 0.2% compressive strain (top). Test load level corresponding to desired test strain level extrapolated from linear preconditioning load-strain relationship (bottom).

low compressive stress levels. Applied stress levels were selected so that the resulting maximum strain ranged from 0.29% and 0.54% (see **Appendix**). (One of the 32 prepared specimens was tested to a high stress level and therefore was not included in any of the statistical analysis.) Nine of the 31 specimens tested at low stress levels were lost due to data acquisition complications (incomplete data were obtained for three specimens due to software malfunctions), saline drip complications (tests were aborted for three specimens due to dehydrated bone or corroding chucks), or operator error (tests were aborted for three specimens due to damaging specimens prior to fatigue testing). Therefore we collected data for and performed statistical analyses on 22 of the 31 specimens tested at low stress levels. After fatigue testing, photographs of the specimens were taken to record typical fatigue fracture patterns.

3.2.3 Measuring Tissue and Apparent Densities

All tissue densities, defined as the microscopic density of the solid bony phase of trabecular bone, and apparent densities, defined as the weight of the fully hydrated bony matrix divided by the specimen volume, were measured after mechanical testing following the lab's standard protocol (OBL SOP #TP_8, Version #1). Bone samples were not taken from within the waisted gage length where trabeculae were fractured as a result of testing to failure. Two bone samples (length, l = 2.5 mm approx.) from just outside the waisted gage length were machined from each of the compound bone/end-cap specimens with a low speed saw (Isomet, Buehler, Corp., Lake Bluff, IL, USA) equipped with a diamond wafering blade operating under copious irrigation. The marrow space contents were removed from the bone samples by ultrasonic agitation with a 1:3 bleach:water solution. After 15-20 minutes of agitation, the cloudy solution was replaced with fresh bleach solution. Ultrasound was continued and the process repeated until the dilute bleach solution remained clear but for no longer than a total of 45 minutes.

The samples were submerged in deionized, distilled water and degassed under vacuum for approximately 30 minutes or until all trapped air bubbles were removed. The samples were weighed while they remained submerged under water to obtained the submerged weight. The bone samples were then centrifuged in vials with dry

gauze for 15 minutes at 1000 RPM (Sorvall Superspeed RC2-B, Ivan Sorvall Inc., Newtown, CT, USA) to remove the water from the pores without drying the bone. Immediately after removing the specimens from the centrifuge, the bone samples were weighed on a digital balance (OHaus Analytical Plus, OHaus Corp, Florham Park, NJ, USA) to obtain the wet weight. Tissue density was calculated as the ratio of wet weight to (wet weight - submerged weight), and apparent density as the ratio of wet weight to sample volume.

3.2.4 Data Analysis

The nomenclature used in this study was consistent with that adopted in the pilot study of this project (Guo, 1993) and defined in the finite element study (Guo *et al.*, 1994). A test was classified as a high-cycle test if the specimen failed after 100 loading cycles ($N_f > 100$ cycles). Conversely, a test was classified as a low-cycle test if the specimen failed before 100 loading cycles ($N_f < 100$ cycles).

The load and deformation data acquired during fatigue tests were processed using RS1 statistical software package (BBN Software Product Corp., Cambridge, MA, USA) to determine the applied stress range $\Delta\sigma$ and resulting strain range $\Delta\epsilon$ for select cycles. The modulus E was calculated as (Fig. 3.5):

$$E = \Delta\sigma / \Delta\epsilon \qquad (3.1)$$

The applied stress range and modulus were each normalized by the initial modulus E_o to reduce scatter in the data due to interspecimen variations in density.

For each specimen, the normalized modulus vs number-of-cycles curve (E/E_o - N) was plotted on linear-log graphs to observe the modulus degradation of the specimen during fatigue. The number-of-cycles that corresponded to a 10% decrease in initial modulus was then determined from this normalized modulus vs number-of-cycles curve for each specimen as the number-of-cycles-to-failure N_f. In 6 of the 22 specimens tested at low stress levels, the last cycle of data acquired by the Interlaken III corresponded to less than 10% decrease in initial modulus, so the number-of-cycles-to-failure was estimated as the number-of-cycles-to-fracture. The modulus

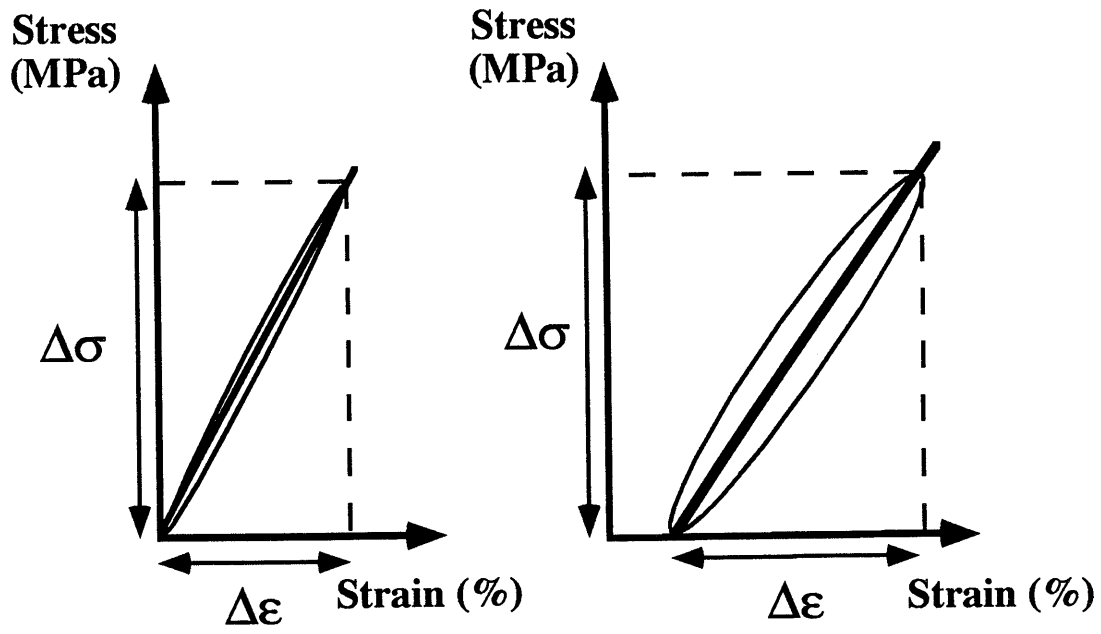

Figure 3.5: Modulus calculated as ratio of applied stress range to resulting strain range for initial (left) and subsequent cycles (right).

degradation of each specimen was also observed by plotting normalized modulus vs life fraction curves (E/E_o - N/N_f) on linear-linear graphs, where life fraction was defined as the current number of cycles divided by N_f.

The normalized applied stress range vs number-of-cycles-to-failure ($\Delta\sigma /E_o$ - N_f) curves for the various groups of data were plotted on log-log graphs. The constants (a, b) of the power law relationship between number-of-cycles-to-failure and normalized applied stress range:

$$(\Delta \sigma /E_o)\ (\%) = a\ (N_f)^{-b} \qquad (3.2)$$

were determined using non-linear regression analysis (power curve fit) of the resulting curves. Equivalently, the constants (log a, b) of the linear relationship between log transformations of the number-of-cycles-to-failure and normalized applied stress range:

$$\log (\Delta \sigma /E_o)\ (\%) = \log a - b \log N_f \qquad (3.3)$$

could have been determined using linear regression analysis. The coefficient b is interpreted as the power of the power law equation (3.2) and as the slope of the linear equation (3.3).

Significant differences in the slopes of the $\log (\Delta \sigma /E_o)\ (\%)$ vs $\log N_f$ curves for the various groups of data were determined using a test of equality of slopes (significance < 0.05) (Neter *et al.*, 1990).

Additional curves were plotted to investigate creep and fatigue behavior previously observed in other creep and fatigue studies. The applied stress range vs resulting strain range for select cycles of specimens were plotted to observe the cyclic response of the bone specimens to fatigue.

The applied stress range vs resulting strain range ($\Delta\sigma$ - $\Delta\epsilon$) for select cycles of specimens were plotted to observe the cyclic response of the bone specimens to fatigue and to quantitatively estimate the contribution of creep damage to the fatigue of trabecular bone by comparing the strain due to creep with the total strain. The strain due to creep ϵ_c was defined as:

$$\epsilon_c = \text{minimum strain at } N_f - \text{minimum strain at cycle 0} \qquad (3.4)$$

The total strain ϵ_T was calculated as:

$$\epsilon_T = \text{maximum strain at } N_f - \text{minimum strain at cycle 0} \quad (3.5)$$

The percentage of strain due to creep % strain $_{creep}$ was calculated based on these strain values and was defined as:

$$\%\ \text{strain}_{creep} = \epsilon_c / \epsilon_T * 100 \quad (3.6)$$

Additionally, strain vs time curves were plotted on linear-linear graphs. Although data was acquired under fatigue, and not creep test conditions, estimated steady state "creep" rates and normalized applied "creep" stress were calculated for comparisons with creep studies on trabecular bone specimens. The steady state "creep" rate was defined as the slope of the strain vs time curve in the central portion of the secondary regime, which was determined by a least-squares, best-fit linear regression of the data within +/- 10% of the midpoint (time to achieve $N_f/2$ cycles) of the secondary regime, based on a definition previously adopted for creep testing of trabecular bone specimens (Bowman *et al.*, 1994). The normalized applied "creep" stress was taken to be the mean normalized applied stress range of the fatigue tests (Fig. 3.6). Log-log plots of the steady-state "creep" rate vs normalized applied "creep" stress, log-log plots of normalized applied "creep" stress vs time-to-failure, and log-log plots of steady-state "creep" rate vs time-to-failure were plotted.

Finally, the 95% confidence interval of experimental data was compared to previously reported finite element model predictions of the creep deformation mechanism and the slow crack growth propagation mechanism for a waisted idealized trabecular bone specimen (Guo, 1993). The slow crack growth model used a two-dimensional honeycomb-like structure made up of an array of hexagonal cells. The cell walls were assumed to be identical linear elastic beams with the mechanical properties of bovine cortical bone (E = 22.6 GPa; Currey, 1984). Each oblique trabeculae had two pre-existing microcracks on the tensile side, located a distance L/4 from the ends. Microcracks were assumed to follow a Beta probability distribution of initial crack lengths, with a maximum crack length of 30% of the thickness of the trabeculae. Initial microcracks were assumed to grow according to the Paris law (Paris and Erdogan, 1963). Struts within the honeycomb were assumed to fracture

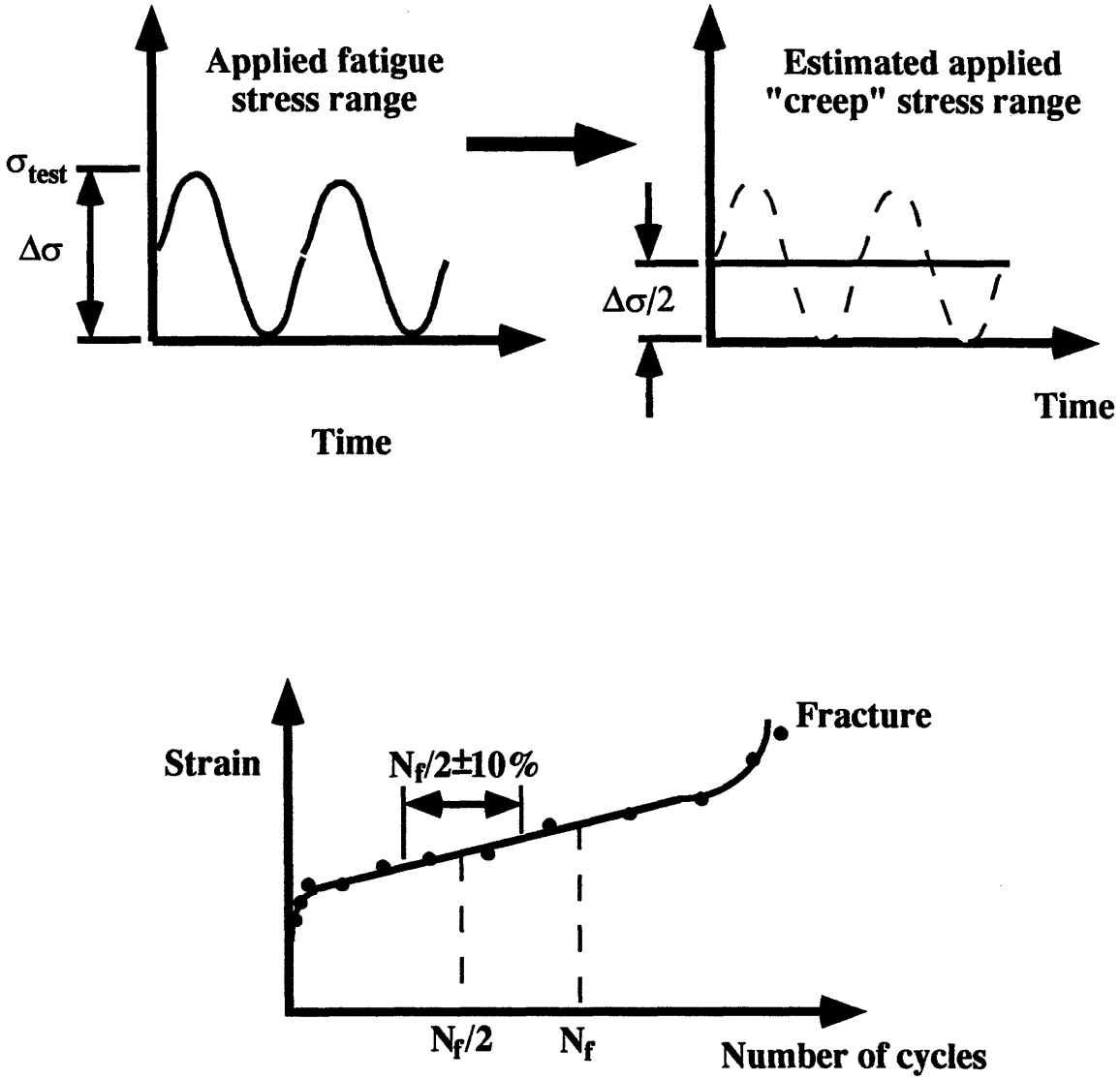

Figure 3.6: Normalized applied "creep" stress (top right) estimated from normalized applied stress rangeof fatigue test (top left). Definition of region for calculating steady-state "creep" rate from the strain versus number of cycles plot (bottom).

when a crack grew to a critical length. After fracture, the strut was removed from the mesh, Young's modulus recalculated, and the simulated cyclic load repeated until fracture of the next strut. The creep model used a single cell analysis based on power-law creep of the bone tissue. Again failure was defined as a 10% reduction in initial Young's modulus. The relative density of the models was 0.3, a value equal to the average relative density of the specimens tested in both fatigue studies of waisted specimens.

3.3 Results

The mean initial secant modulus Eo of all 22 specimens was 2900 MPa (SD 838, range = 1258 - 4248 MPa). The mean apparent density was 0.56 g cc^{-1} (SD 0.11, range = 0.34 - 0.75). The mean tissue density was 1.90 g cc^{-1} (SD 0.25, range = 1.16 - 2.52). The mean relative density was 0.30 (SD 0.068, range = 0.18 - 0.48).

Linear regression analysis of the high-cycle data acquired from this study indicated that there was a strong ($r^2 = 0.64$) and significant ($p < 0.0001$) linear relationship between the log applied stress range normalized by the initial Young's modulus (log ($\Delta \sigma / E_o$) (%)) and log number-of-cycles-to-failure (log N_f) (Fig. 3.7):

$$\log (\Delta \sigma / E_o) (\%) = -0.17 - 0.062 \log N_f \qquad (n = 22) \qquad (3.7)$$

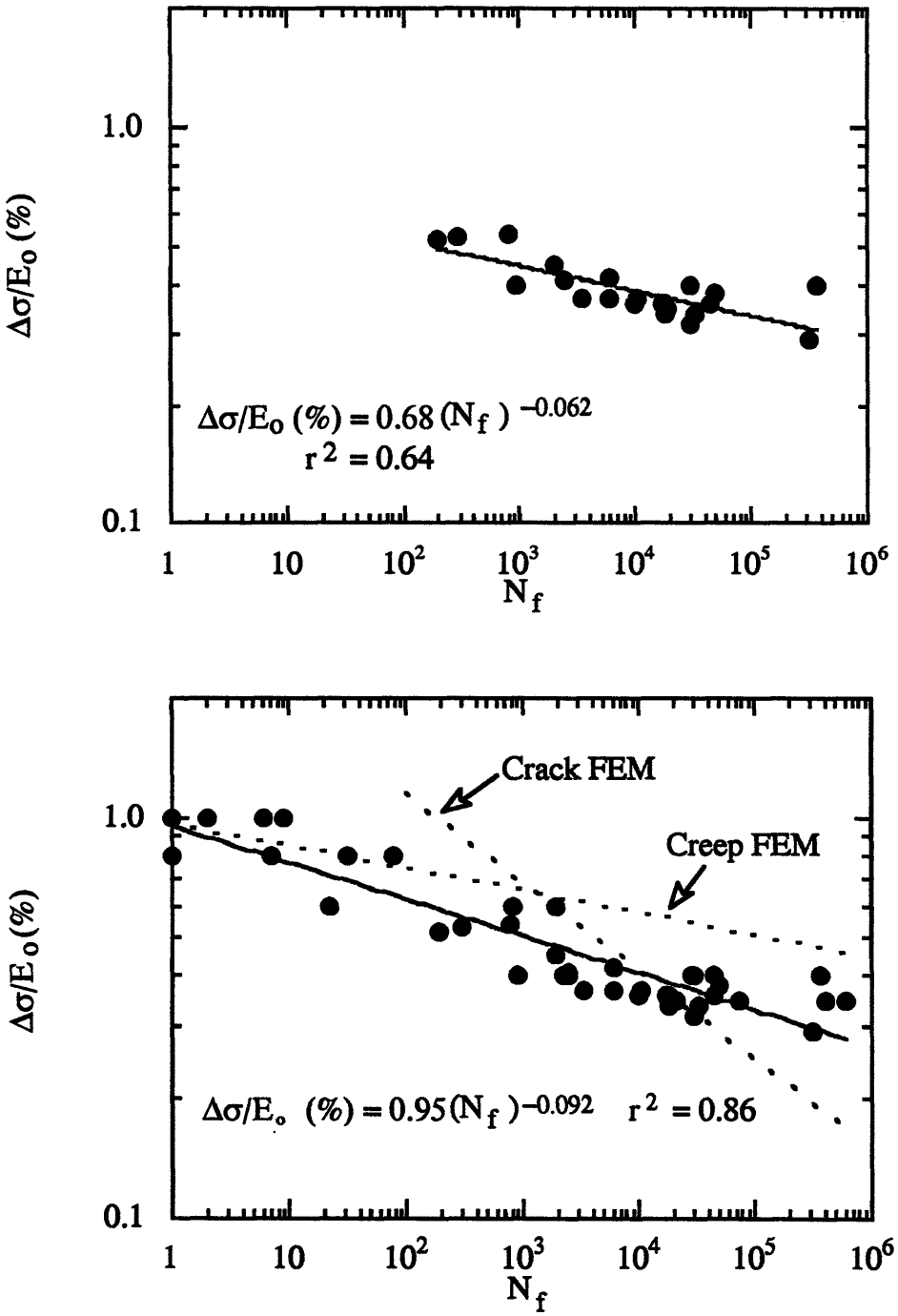

Figure 3.7: Normalized stress range vs number-of-cycles-to-failure for high-cycle data from the current study (top).
Comparison of the finite element creep model and the crack propagation model with the power curve fit of the pooled data from the current and the pilot study (Guo, 1993) (bottom).

Statistically significant ($p < 0.0001$) high negative correlation power curve fits were also found when high-cycle data from this study and high-cycle data from the pilot study were plotted as a single data group ($r^2 = 0.53$), and when low-cycle data from the pilot study, high-cycle data from this study, and high-cycle data from the pilot study were plotted as a single data group ($r^2 = 0.86$) (Table 3.1)

Table 3.1. *Slopes and intercepts from fatigue experiments*

$$\log (\Delta \sigma / E_o) (\%) = \log a - b \log N_f$$

data group	**b**	**signif. level of b**	**a**	**signif. level of a**	**r^2**
low-cycle from pilot n= 9	0.054	0.19	-0.022	0.61	0.24
high-cycle from current n = 22	0.062	0.0001*	-0.17	0.002*	0.64
high-cycle from pilot and current n = 32	0.062	0.0001*	-0.15	0.001*	0.53
low-cycle from pilot and high-cycle from pilot and current n = 41	0.092	0.0001*	-0.022	0.37	0.86

* statistical significance ($p < 0.05$)

The difference between the slopes of the high-cycle data from this study and that of the high-cycle data from the pilot study was not statistically significant ($p > 0.5$) as determined by a test of equality of slopes so the high-cycle data were pooled, satisfying one of the study's original objectives. The difference between the slopes of the pooled high-cycle data and the low-cycle data was very small relative to the value of the slopes themselves (Δb in Table 3.2), and to their pooled standard deviation (error in our ability to predict the slope) (% SEE in Table 3.2). The slopes of the low- and the high-cycle regimes of the log normalized applied stress range versus the

log number-of-cycles-to-failure curve was not significantly different ($p > 0.05$; $|t^*| < 1.96$) as determined by a test of equality of slopes performed on the null hypothesis that slope of low-cycle data = slope of the pooled high-cycle data. Thus, low-cycle data and the pooled high-cycle data were also pooled together to from a single data group. Furthermore, a single linear function relates the log normalized applied stress to the log number-of-cycles-to-failure along the entire normalized stress range tested in both studies.

Table 3.2. *Comparison of slopes with low-cycle data*

$$\log (\Delta \sigma / E_o) (\%) = \log a - b \log N_f$$

data group	**b** slope	**Δ b** $b_{\text{data group}} - b_{\text{low-cycle}}$	**% SEE**	**p value†**	**t* value†**
high-cycle from current	0.0622	-0.00734	9	> 0.5	-0.237
high-cycle from pilot and current	0.0608	-0.00599	7	> 0.5	-0.187

† Test of equality of slopes (Ho: slope of low-cycle data = slope of **data group**)

* statistical significance ($p < 0.05$ or $|t^*| > 1.96$)

Previously reported finite element predictions of the slope of $\log (\Delta \sigma / E_o)$ (%) vs $\log N_f$ for both a creep model and a slow crack growth propagation model (Guo 1993) did not fall within the 95% confidence interval of the experimentally derived pooled data plotted on $\log (\Delta \sigma / E_o)$ (%) vs $\log N_f$ curves (Fig. 3.7). The intercept of the creep finite element model agreed well with the power curve fit of the pooled data, while the slopes predicted by both the crack propagation and creep analysis models and the intercept of the crack propagation model did not.

Nine of the 22 specimens tested at low stress levels exhibited negligible change in modulus during the initial half of the specimen's fatigue life followed by a continuous decrease in modulus until fracture. Six of the 22 specimens demonstrated a continuous decrease in modulus from the beginning. Seven of the 22 specimens exhibited negligible change in modulus, then an atypical sudden increase in modulus, followed by a continuous decrease in modulus at the typical rate. These three

behavior patterns of estimated creep strain were observed at all applied normalized stress ranges tested (Figs. 3.8a, b).

The stress-strain loops of fifteen of the 22 specimens tested at low stress levels exhibited increasing non-linearity and hysteresis and decreasing secant modulus (Figs. 3.9a, b). The stress-strain loops of these fifteen specimens translated along the direction of increasing strain from an initial strain of 0.0% (at -10 N compressive load) to a mean strain due to creep ϵ_c of 0.10% (SD 0.059%, range = 0.035% - 0.23%) and a mean total strain ϵ_T of 0.51% (SD 0.13%, range = 0.40% - 0.76%) (Fig. 3.9). The mean percentage of strain due to creep % strain $_{creep}$ was 19.5% (SD 9.93%, range = 8.1% - 36.1%) (Fig. 3.9).

From the estimated creep strain-time plots, 13 of the 22 specimens tested at low stress levels demonstrated the classical rapid primary, slow secondary, and rapid tertiary regimes of creep (Fig. 3.10a, b). Four of the 22 specimens did not exhibit a change in steady state creep in the secondary regime. Five of the 22 specimens that exhibited the atypical sudden increase in modulus also exhibited an atypical decrease in steady state creep strain. These three behavior patterns of estimated creep strain were observed at all applied normalized stress ranges tested. Strong and significant power law relationships were found between steady-state "creep" rates and normalized "creep" stress (Fig. 3.11), between normalized applied "creep" stress and time-to-failure (Fig. 3.11) and between steady-state "creep" stress and time-to-failure (Fig. 3.11).

3.4 Discussion

Previous investigators observed distinctly different fatigue behavior of trabecular bone in the low-cycle and high-cycle range and suggested that trabecular bone fails by creep in the low-cycle regime and by microcrack damage accumulation in the high-cycle fatigue regime (Michel *et al.*, 1993). Our compressive fatigue experiments on specimens of devitalized trabecular bone do not reveal distinct low and high cycle regimes. A single linear function relates the log normalized applied

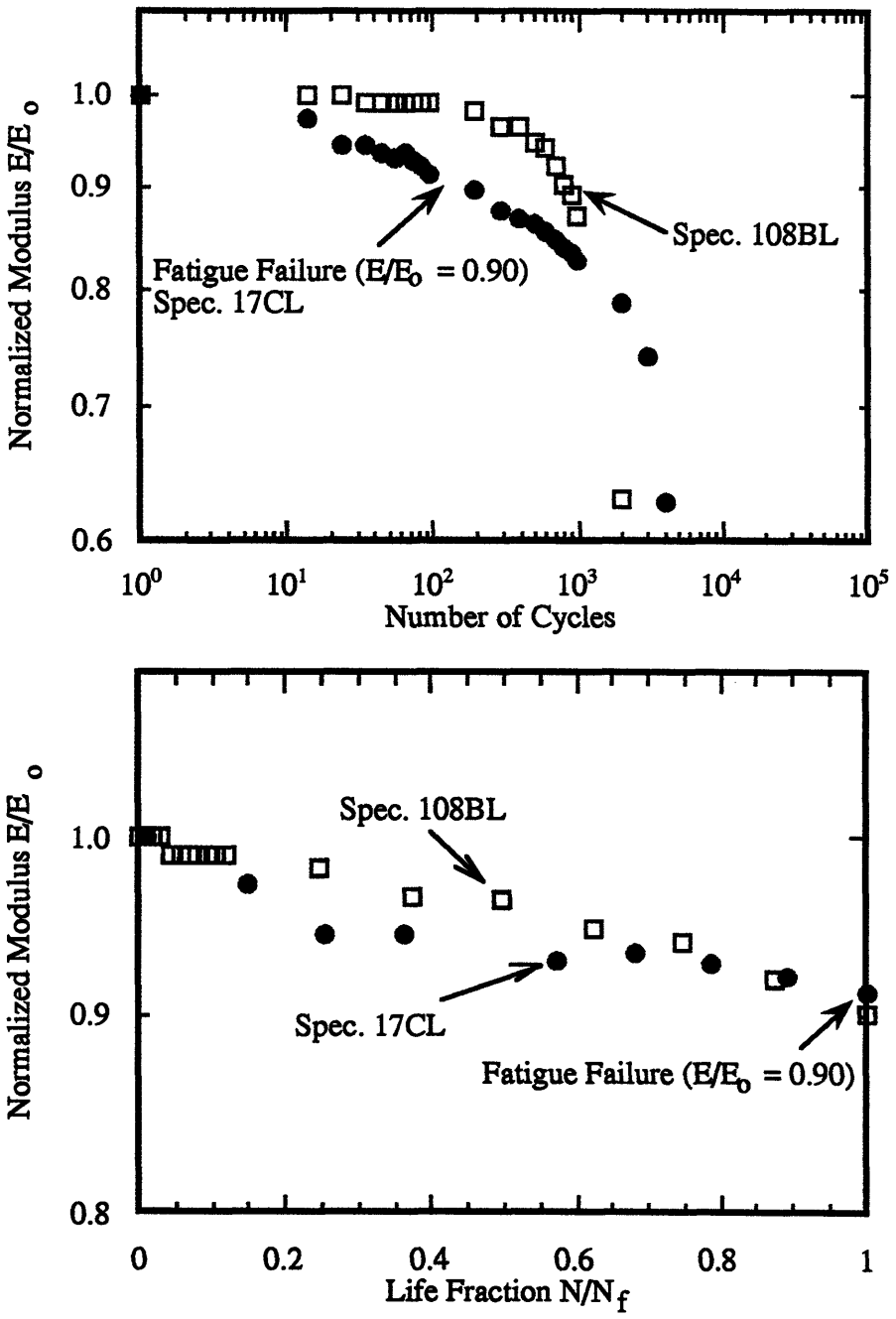

Figure 3.8: (a) Examples of two of the modulus degradation patterns exhibited by specimens. Both specimens shown here failed after approximately 200 cycles. Spec. 17CL demonstrated continuous decrease in modulus until fracture (top). 108BL demonstrated negligible change in modulus followed by a continuous decrease in modulus until fracture (top). Same modulus degradation data plotted as normalized modulus vs life fraction (bottom)..

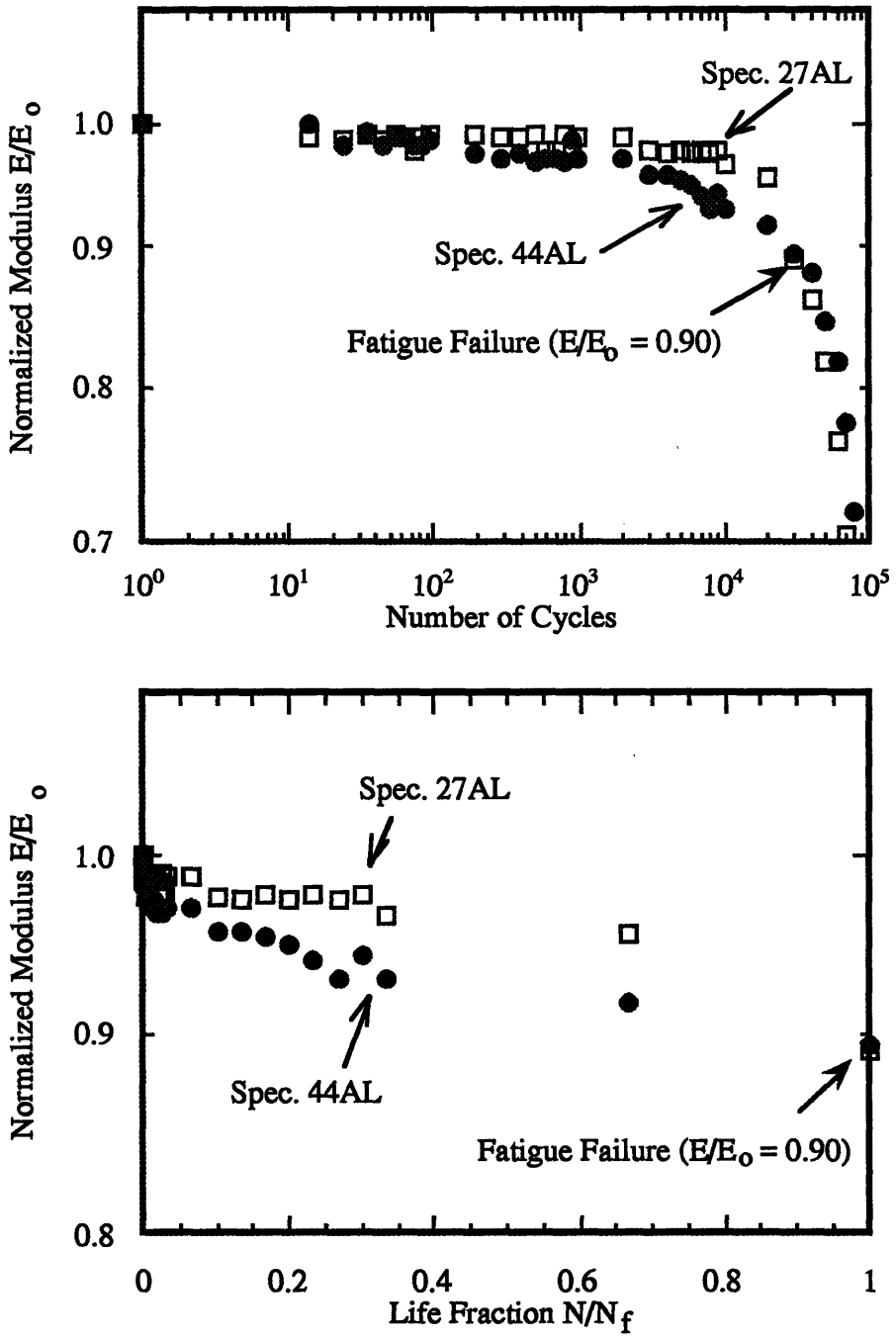

Figure 3.8: (b) Same modulus degradation patterns as in Fig. 3.8 (a), but the specimens shown here failed after approximately 30,000 cycles. Spec. 44AL demonstrated continuous decrease in modulus until fracture (top). Spec. 27AL demonstrated negligible change in modulus followed by a continuous decrease in modulus until fracture (top). Same modulus degradation data plotted as normalized modulus vs life fraction (bottom).

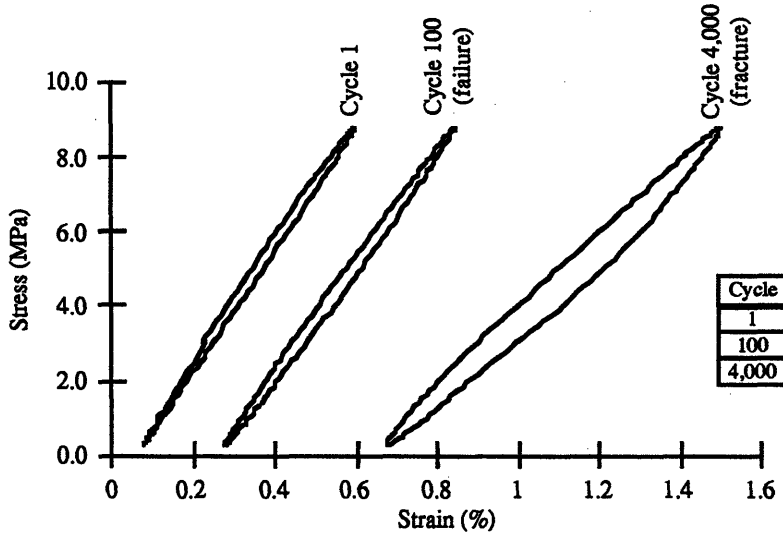

Cycle	Min Strain(%)	Max Strain(%)
1	0.078	0.59
100	0.27	0.84
4,000	0.67	1.5

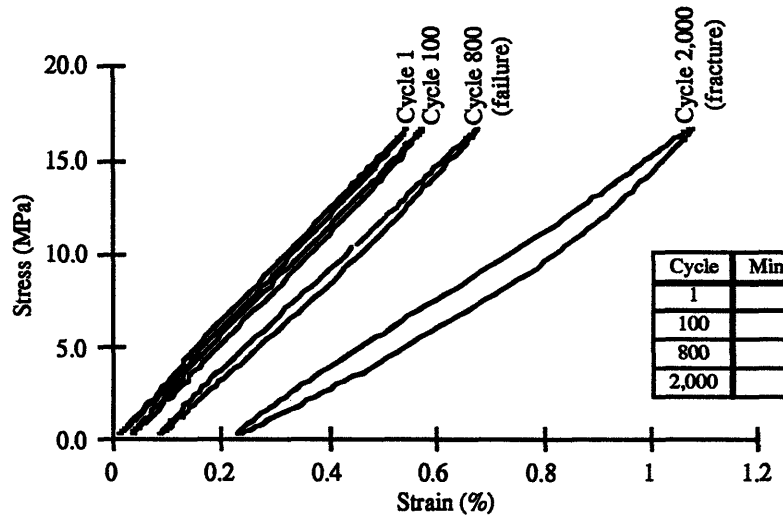

Cycle	Min Strain(%)	Max Strain(%)
1	0.01	0.55
100	0.034	0.58
800	0.083	0.68
2,000	0.23	1.08

Figure 3.9a: Stress-strain loops exhibited increasing non-linearity and hysteresis and decreasing secant modulus. Both specimens (Spec. 17CL top and Spec. 108BL bottom) had approximately equal fatigue lives (Nf = 200) but different minimum strain (%) at failure. The data shown in Fig. 3.8a and 3.9a correspond to the same specimens.

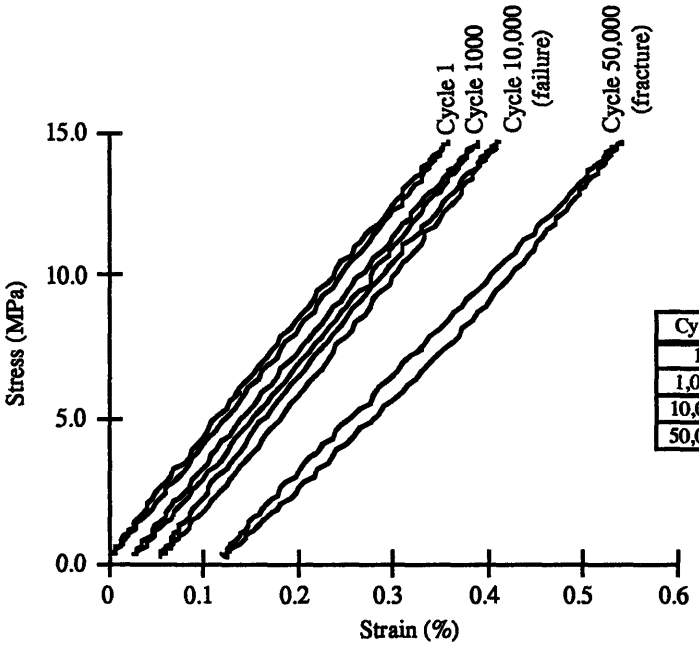

Cycle	Min Strain(%)	Max Strain(%)
1	0.002	0.36
1,000	0.025	0.39
10,000	0.054	0.41
50,000	0.12	0.54

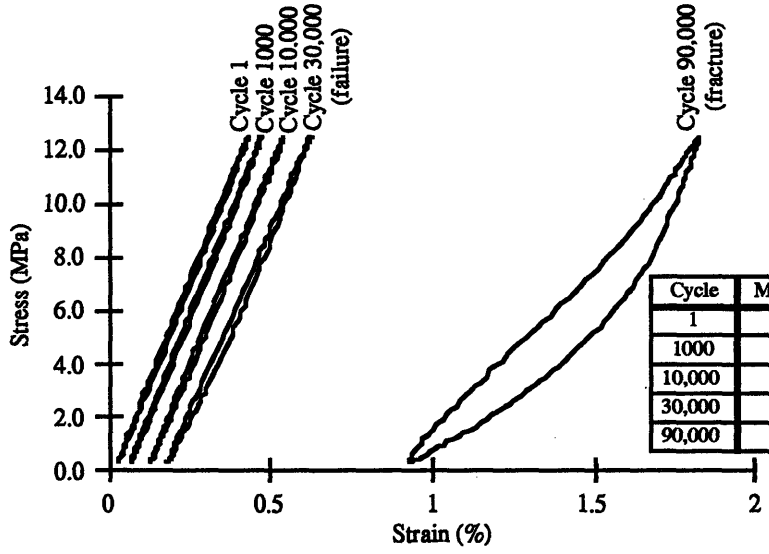

Cycle	Min Strain(%)	Max Strain(%)
1	0.03	0.43
1000	0.07	0.47
10,000	0.13	0.54
30,000	0.18	0.63
90,000	0.93	1.83

Figure 3.9b: Stress-strain loops exhibited increasing non-linearity and hysteresis and decreasing secant modulus. Both specimens (Spec. 44AL top and Spec. 27ALbottom) had approximately equal fatigue lives (Nf = 20,000) but different minimum strain (%) at failure. The data shown in Figures 3.8b and 3.9b correspond to the same specimens.

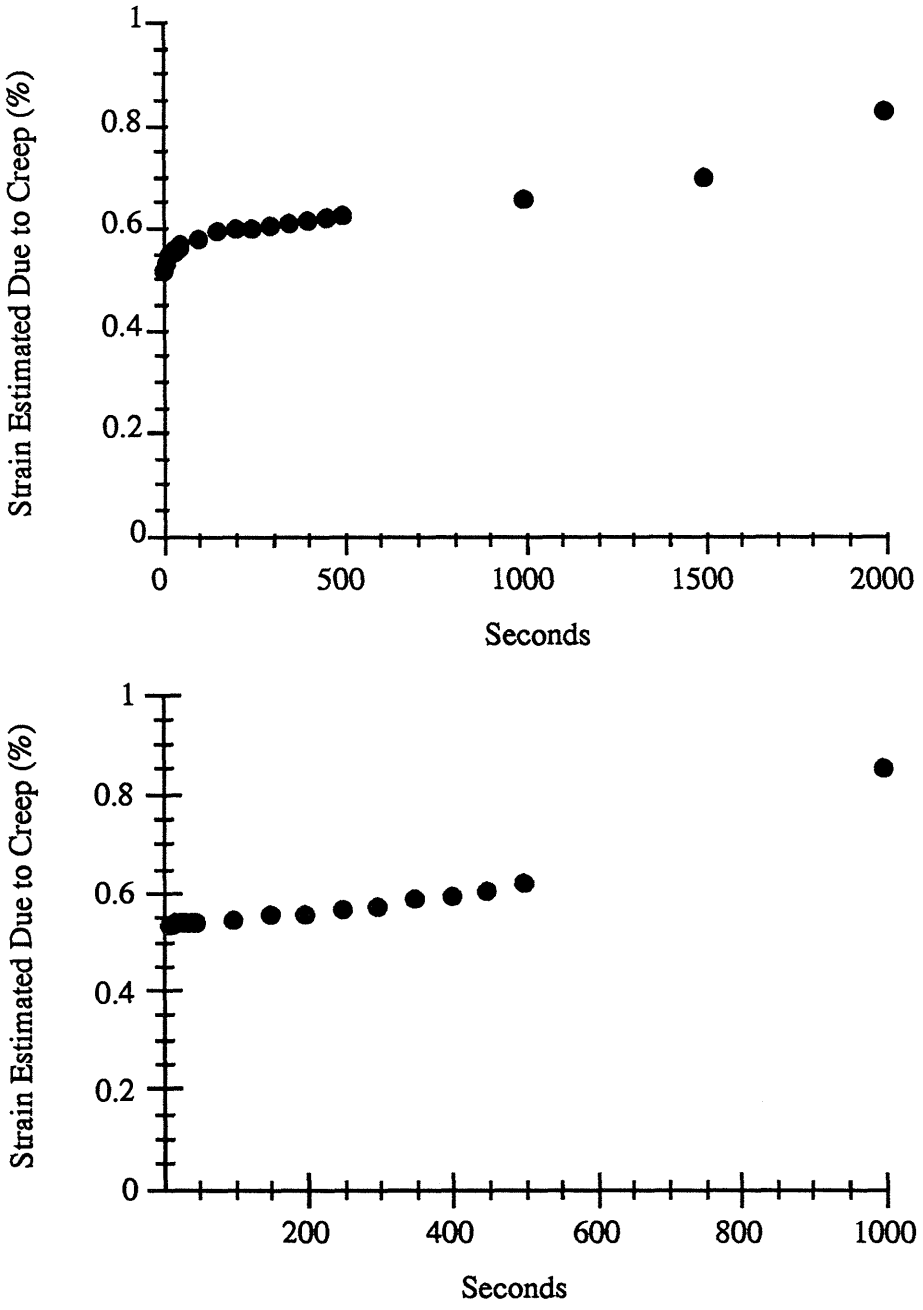

Figure 3.10: (a) Examples of typical specimens that demonstrated the the classical rapid primary, slow secondary, and rapid tertiary regimes of creep (Spec. 17CL top and Spec. 108BL bottom). The initial normalized stress of both specimens was 0.53%. The data shown in Fig. 3.8a, 3.9a, and 3.10a correspond to the same specimens.

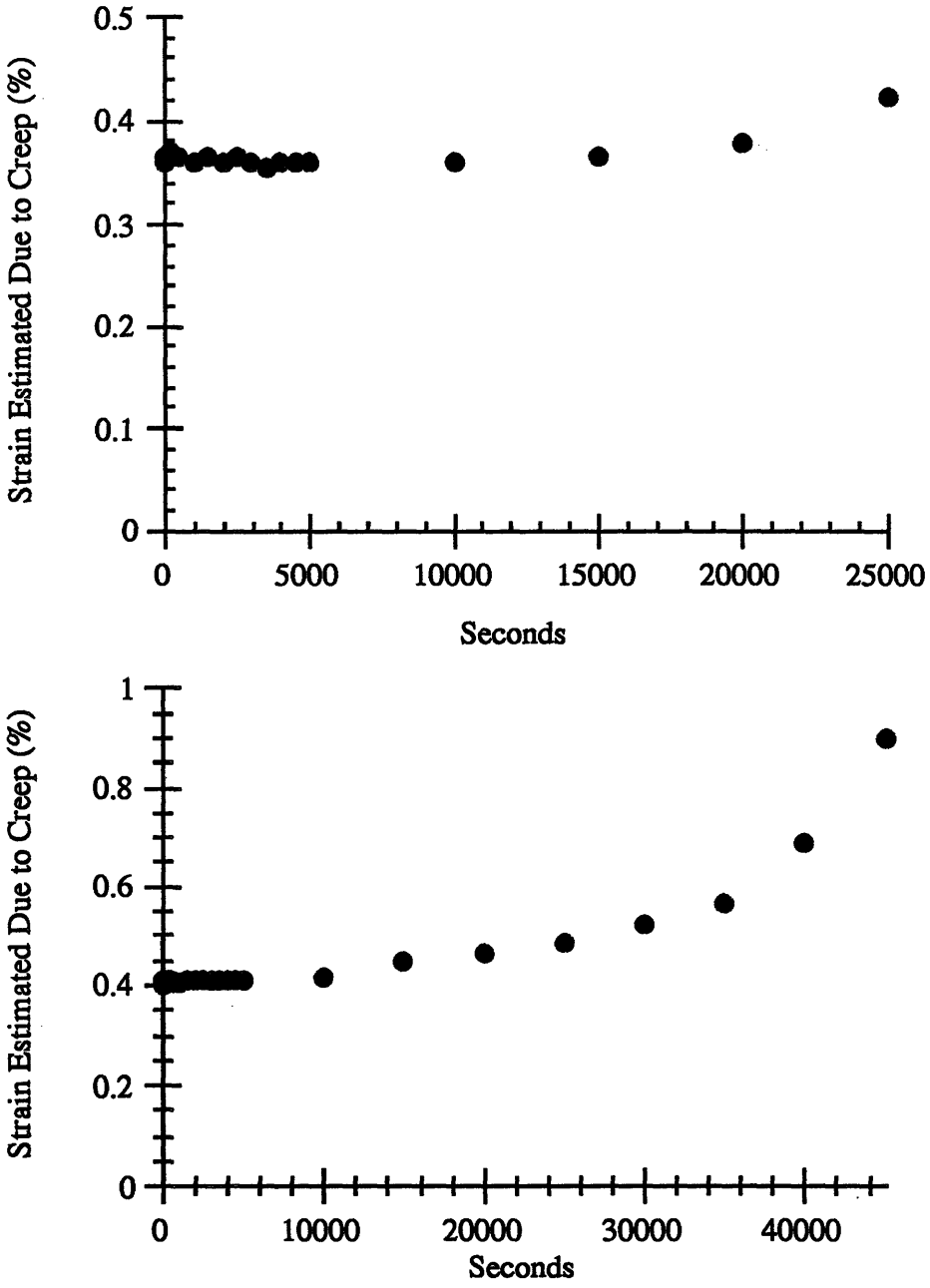

Figure 3.10b: More examples of typical specimens that demonstrated the classical rapid primary, slow secondary, and rapid tertiary regimes of creep (Spec. 44AL top and Spec. 27AL bottom). The initial normalized stress of both specimens was 0.38%. Data shown in Figs. 3.8b, 3.9b, and 3.10b correspond to the same specimens.

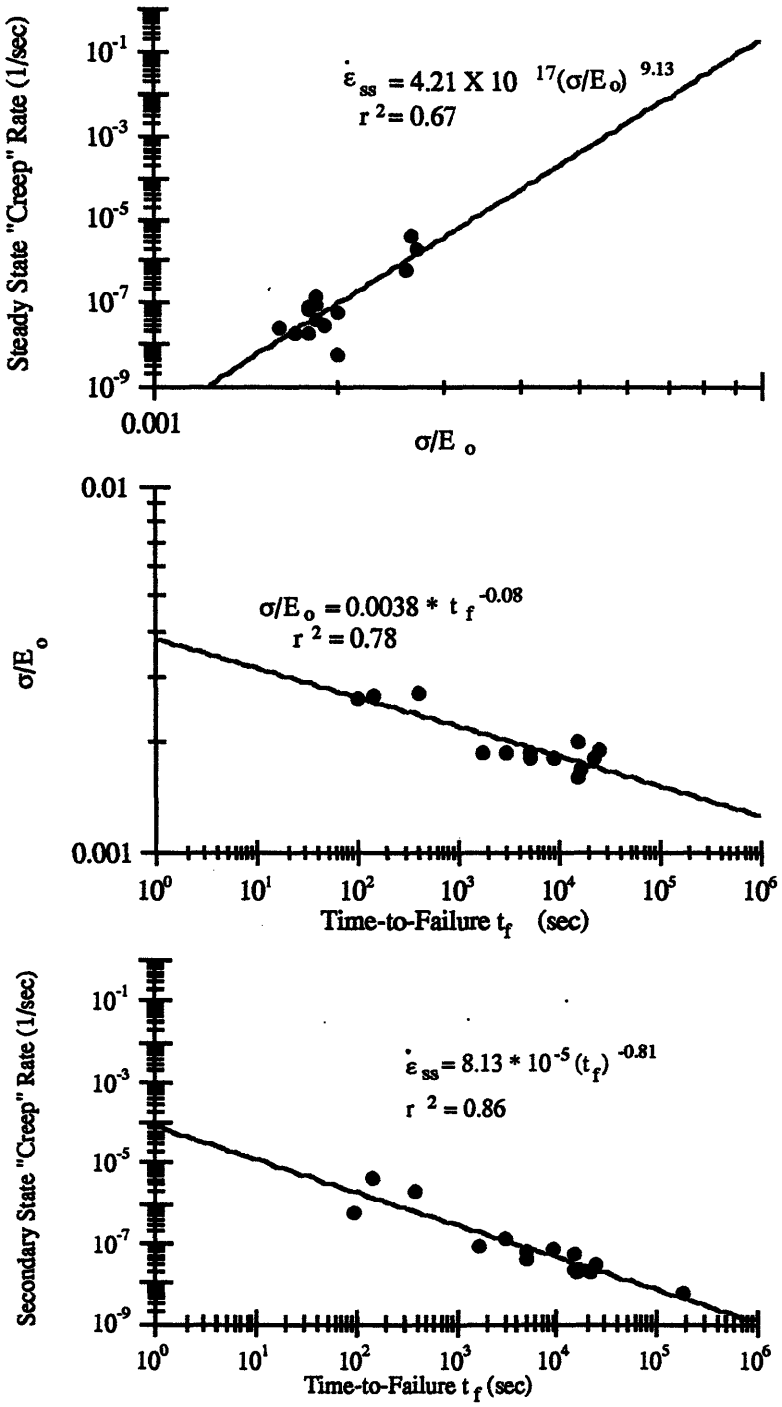

Figure 3.11: Log-log plot of steady-state "creep" rate vs applied normalized stress (top). Log-log plot of applied normalized stress vs time-to-failure (middle). Log-log plot of secondary-state "creep" rate vs time-to-failure (bottom).

stress to the log number-of-cycles-to-failure along the entire normalized stress range tested. The slope of this function lies between those expected from modelling creep and slow crack growth (Guo, 1993). fatigue damage may be caused by some combination of these two mechanisms or by additional, as yet unmodelled, mechanisms, such as creep buckling.

As in previous studies, we qualitatively observed significant creep behavior in the majority of the specimens as demonstrated by the progressive translation of the hysteresis loop along the strain axis and by increasing strain in the secondary regime of the estimated creep strain-time plots. We have quantitatively estimated the contribution of creep damage to the fatigue of trabecular bone by comparing the estimated strain due to creep with the total strain. In addition to creep behavior, we observed possible slow crack growth behavior over the secondary regime of those specimens where there was a gradual decrease in normalized modulus but no change in strain with increasing cycles of loading. Additionally, microscopic examination of fatigue damaged specimens from the pilot study showed localized fractures and delaminations of individual trabeculae, suggesting that microcrack propagation could be one of the possible damage mechanisms (Guo, 1993). The qualitative and quantitative experimental evidence of creep and slow crack growth throughout the stress ranges tested suggest that both mechanisms are contributing to the damage mechanism to some degree. In addition, comparisons of our experimental data with predictions from finite element models of creep deformation and slow crack growth strongly suggest that neither damage mechanism alone is responsible for fatigue.

3.4.1 Strengths

Increased predictive power of derived power-law equation. In this study we employed a testing protocol that used cylindrical specimens with a reduced-section in which strain is measured directly with a miniature extensometer (Keaveny *et al.*, 1994). Additionally, we culled and tested only homogenous specimens whose longitudinal axes were aligned with the principal material axes. We have validated this procedure for harvesting trabecular bone to yield homogeneous specimens (Chapter 2). The testing of homogeneous and well-aligned specimens minimizes

scatter in the linear regression of the log applied normalized stress range vs log number-of-cycles-to-failure curve as reflected in the very high negative correlation value ($r^2 = 0.84$, pooled data). Reduced scatter thereby increases the predictive power of the derived linear equation.

Pooled data. This study was expressly designed so that acquired data could be pooled with data from a pilot study (Guo, 1993). To minimize inter-study variability, specimens were selected and tested following the same protocols as in the pilot study. It should be noted that there was no significant difference ($p > 0.5$) between the slopes of the log applied normalized stress range vs log number-of-cycles-to-failure curve of the two studies as determined by the test of equality of slopes, and both sets of data were pooled.

3.4.2 Limitations

The finite element models used for comparisons with the experimental data make idealized assumptions of trabecular architecture. The slow crack growth propagation model uses a honeycomb array of identical hexagonal cells and the creep model uses a single hexagonal unit cell. The models assume constant wall thickness which poorly represent the trabecular architecture. Because the honeycomb deforms by the same mechanisms as trabecular bone, we expect that the honeycomb analysis is capable of qualitatively describing the slow crack growth and power law creep in trabecular bone. In addition, material parameters used to determine the rate of crack propagation and power law creep within a trabecula are poorly described. The parameters of Paris Law and power law creep for trabecular tissue are unknown and were assumed to be the same as those previously determined for bovine cortical bone. However, these models made adequate and robust predictions of the number of cycles to failure of trabecular bone cubic specimens.

Although the experimental data of this study suggest that the fatigue mechanisms may involve a combination of creep and slow crack growth propagation, this study was not designed to determine the relative contribution of the two mechanisms to the fatigue damage process. Additionally, this study did not account for potential *in vivo* adaptive and repair responses to fatigue damage. Thus, the *in*

vitro fatigue properties determined in this study should provide a lower bound on the fatigue properties *in vivo* as bone remodels continuously *in vivo*.

Experimental data was compared with finite element predictions of only the creep deformation and slow crack growth propagation mechanisms. Data must be compared with finite element predictions made by other possible damage mechanism models such as creep buckling and creep fracture, for example.

3.4.3 Comparisons with Previous Studies

Comparison with fatigue of cubic specimens. Our fatigue data on waisted specimens do not agree with those obtained from a previously reported fatigue study of cubic trabecular bone specimens (Michel *et al.*, 1993), suggesting that the observed mechanical behavior of trabecular bone to fatigue depends on the test protocol. That study demonstrated distinctly different modulus degradation with the number of cycles for high-cycle and low-cycle fatigue. This observation suggested that two separate damage mechanisms, fatigue and creep damage accumulation, may occur during fatigue of cubic trabecular bone specimens in the low and high stress regime, respectively. Different relationships between normalized applied stress range and number-of-cycles-to-failure (S-N) were obtained in the cubic and waisted studies. The high negative (r^2 = 0.72) and very high negative (r^2 = 0.84) correlation values for the cubic (Michel *et al.*, 1993) and waisted studies, respectively indicate that the number-of-cycles-to-failure can be predicted fairly accurately from a knowledge of the initial normalized applied stress range and the experimental setup (cubic vs waisted). The different observed responses to fatigue by cubic and waisted specimens of trabecular bone may be due to compliant end-effects present in cubic but not in waisted specimens. Compliant end-effects are the result of cutting the layer of trabeculae at the surface during specimen preparation. The ends of the surface trabeculae in contact with the platen are relatively free, rather than restrained by the adjacent trabeculae, thereby reducing the stiffness of the surface layer relative to underlying layers (Odgaard and Linde, 1991).

Two observed phenomena in compressive fatigue experiments of cubic specimens may be attributed to these compliant end-effects. First, the initial increase

in modulus may reflect the progressive loss of the compliant end layer as the specimen is repeatedly loaded (Michel *et al.*, 1993). Second, the distinctly different response to compressive fatigue in the low-and high-cycle regimes may reflect varying contributions of creep to the damage process. In addition to performing fatigue tests of cubic specimens, Michel and Guo (1993) examined the local strain distributions over a range of applied maximum global strains. They observed inhomogeneous local strain distributions with higher local strains near the ends of the specimens. In the case of low applied global strain, local strains in the middle of the specimen were very low (< 0.5%) (Guo, 1993). A creep threshold around 0.5%, below which creep does not occur has been determined for bovine cortical bone (Fondrk *et al.*, 1988). The existence of a creep threshold of similar magnitude in bovine trabecular bone would prevent creep from occurring in the middle of the specimen and limit contribution of creep to the damage process.

Because no increase in the initial modulus was observed during the fatigue of waisted specimens, it is believed that end artifacts such as those due to compliant end-effects have been minimized. Presumably, fatigue damage is occurring predominantly in the central waisted region where local strains are much higher than at the ends of the specimen. Although the local strain distribution along the axial direction of the waisted region has not been measured, this strain distribution is likely to be more uniform than that along the entire length of the cubic specimen (Guo, 1993). Thus, the creep process may be more uniformly distributed along the axial direction of the waisted region.

Comparison with pilot fatigue data on waisted specimens. Two of the modulus degradation patterns observed in this study were similar to the two reported in the pilot study of waisted specimens. The pilot study reported different patterns for low and high-cycle fatigue, with the low-cycle case demonstrating a continuous drop in the modulus and the high-cycle case demonstrating a minimal initial change followed by a rapid drop in modulus. We believe that the behaviors are more similar than different when the modulus degradation pattern and total number-of-cycles-to-failure are considered together. Data plotted on linear-log scales and at logarithmic

time points (as in the pilot study and in Fig. 3.8 top) create the illusion that a decrease in modulus occurs earlier and over a greater number of cycles in a low-cycle test than a high-cycle test: however, the number of cycles during which the modulus decreases relative to the number-of-cycles-to-failure are approximately equal in both cases. Linear-linear graphs of normalized modulus vs life fraction curves demonstrate that the modulus degradation patterns are similar (Fig. 3.8 bottom). Additionally, we found these two patterns at all stress levels of tests and not correlated to the stress level of the fatigue test. The similarity in modulus degradation patterns along the entire stress range tested provides further support that the damage mechanism is not dominated by different mechanisms on different cycle regimes.

3.4.4 Future Directions

The observed differences in the fatigue behavior of cubic and waisted specimens of bovine trabecular bone may be critical for interpreting existing fatigue literature. One important objective would be to further investigate the hypothesized differences in strain distributions between the waisted and cubic specimens. Assumptions that the local strain distribution is more uniform along the axial direction of the waisted region should be validated. Optical measurements of the local strain distribution similar to those made in the fatigue study of cubic specimens could be conducted on waisted specimens under uniaxial compression. The local strain distributions of waisted specimens could be compared with those found for the cubic specimens.

Additional compressive fatigue tests of waisted trabecular bone at extremely low initial normalized stress levels (< 0.35%) may reveal a stress threshold below which creep does not occur and a transition point at which slow crack growth propagation begins to dominate the fatigue damage process. The degree to which slow crack growth propagation occurs a progressively lower stress levels can be investigated by additional testing and quantified through more finite element modeling.

Our comparisons with existing finite element predictions made by creep

deformation and slow crack growth propagation models (Guo, 1993) indicate that the fatigue damage mechanisms may not be just creep or slow crack growth propagation alone. To reveal the fatigue failure mechanism of waisted specimens of trabecular bone would require modeling other possible deformation modes. Our previous discussion of the experimental data strongly suggests investigating a creep buckling model that would incorporate existing creep buckling analyses found in aeronautics literature for mechanical structures (Hoff, 1954). Additionally, a creep fracture model may lend insight to the fatigue failure mechanism. The ideal model would combine both creep deformation and slow crack growth mechanisms. Such a model could be designed by modifying the existing slow crack growth model so that cell wall material would behave like a creeping beam rather than the current assumption that the cell wall is linearly elastic to fracture. By then assuming various thicknesses of the individual oblique trabeculae, each beam would creep at a different rate. Models that more accurately represent the general features of trabecular bone architecture, such as a Voronoi honeycomb model may also prove fruitful. After generating additional finite element models of possible damage mechanisms, the experimental data can be compared with the models' predictions.

3.5 Conclusions

In conclusion, our compressive fatigue experiments on specimens of devitalized trabecular bone do not reveal distinct low- and high-cycle regimes. A single linear function relates the log normalized applied stress to the log number-of-cycles-to-failure along the entire normalized stress range tested. The slope of this function lies between those expected from modelling creep and slow crack growth (Guo, 1993). Fatigue damage may be caused by some combination of these two mechanisms or by additional, as yet unmodelled, mechanisms, such as creep buckling or creep fracture.

Chapter 4

Conclusions and Future Directions

In this study, we first validated the use of contact radiography in selecting trabecular bone specimens of homogeneous density whose longitudinal axis is aligned with the principal trabecular orientation. Although previous investigators have observed a wide variation in orientation over small regions of trabecular bone, our micro-magnetic resonance imaging results indicate that our current selection technique using contact radiographs ensured an acceptable degree of misalignment between the principal trabecular orientation and the longitudinal axis of the specimen.

After validating the specimen selection technique, we applied the technique when selecting specimens for mechanical testing aimed at accurately characterizing the compressive fatigue behavior of devitalized bovine trabecular bone. Specimens were tested under loads corresponding to low stress levels normalized by the initial modulus and data was pooled with previously reported pilot data (Guo, 1993). Previous investigators observed distinctly different fatigue behavior of trabecular bone in the low-cycle and high-cycle range and suggested that trabecular bone fails by creep in the low-cycle regime and by microcrack damage accumulation in the high-cycle fatigue regime (Michel *et al.*, 1993). Our compressive fatigue experiments on specimens of devitalized trabecular bone do not reveal distinct low and high cycle regimes. A single power function relates the normalized applied stress to the number-of-cycles-to-failure along the entire normalized stress range tested. The exponent of this function lies between those expected from modelling creep and slow crack growth (Guo, 1993). Fatigue damage may be caused by some combination of these two mechanisms or by additional, as yet unmodelled, mechanisms, such as creep buckling or creep fracture.

References

Ashman, R.B., Corin J.D., Turner, C.H. (1987) Elastic properties of cancellous bone: measurement by an ultrasonic technique. *J. Biomech.* **20**:979-986.

Ashman, R.B., and Rho, J.Y. (1988) Elastic modulus of trabecular bone material. *J. Biomech.* **21**:177-181.

Ashman, R.B., Rho, J.Y., Turner, C.H. (1987) Anatomical variation of orthotropic elastic moduli of the proximal human tibia. *J. Biomech.* **22**:895-900.

Benaissa, R., Uhthoff, H.K., and Mercier, P. (1989) Repair of trabecular fatigue fractures. Cadaver studies of the upper femur. *Acta. Orthop. Scand.*, **60**:585-589.

Bensusan J.S., Davy D. T., Heiple K.G., Verdin P.J. (1983) Tensile, compressive and torsional testing of cancellous bone. *Trans. 29th Orthop. Res. Soc.*, **8**:132.

Borchers, R.E. (1991) Multiaxial failure criteria for trabecular bone. Master's thesis, Massachusetts Institute of Technology, Cambridge, MA.

Bowman, S.M., Keaveny, T.M., Gibson, L.J., Hayes, W.C., and McMahon, T.A. (1994) Compressive creep behavior of bovine trabecular bone. *J. Biomech.* **27** (3):301-310.

Brown, T.D. and Ferguson, A.B. (1980) Mechanical property distributions in the cancellous bone of the human proximal femur. *Acta. Orthop. Scand.*, **51**:429-437.

Burr, D.B., Martin, R.B., Schaffler, M.B., and Radin, E.L. (1985) Bone remodeling in response to in vivo fatigue microdamage. *J. Biomech.* **18**:189-200.

Caler, W.E. and Carter, D.R. (1989) Bone creep-fatigue damage accumulation. *J. Biomech.* **22**:625-635.

Carter, D.R. and Caler, W.E. (1985) A cumulative damage for bone fatigue. *J. Orthop. Res.* 3:84-90.

Carter, D.R. and Caler, W.E. (1983) Cycle-dependent and time-dependent bone fracture with repeated loading. *J. Biomech. Engineering* **105**:166-170.

Carter, D.R., Caler, W.E., Spengler, D.M., and Frankel, V.H. (1981a) Fatigue behavior of adult cortical bone: the influence of mean strain and strain range. *Acta. Orthop. Scand.* **52**:481-490.

Carter, D.R., Caler, W.E., Spengler, D.M., and Frankel, V.H. (1981b) Uniaxial fatigue of human cortical bone. The influence of tissue physical characteristics. *J. Biomech.* **14**:461-470.

Carter, D.R. and Hayes, W.C. (1976a) Bone compressive strength: the influence of density and strain rate. *Science,* **194**:1174-1176.

Carter, D.R. and Hayes, W.C. (1976b) Fatigue life of compact bone--I. Effects of stress amplitude, temperature and density. *J. Biomech.,* **9**:27-34.

Carter, D.R., Hayes, W.C., and Schurman, D.J. (1976c) Fatigue life of compact bone--II. Effects of microstructure and density. *J. Biomech.,* **9**:211-218.

Carter, D.R. and Hayes, W.C. (1977a) Compact bone fatigue damage--I. Residual strength and stiffness. *J. Biomech.,* **10**:325-337.

Carter, D.R. and Hayes, W.C. (1977b) Compact bone fatigue damage: a microscopic examination. *Clin. Orthop.,* **127**:265-274.

Carter, D.R. and Hayes, W.C. (1977c) The compressive behavior of bone as a two-phase porous structure. *J. Bone Joint Surg.,* **59**:954-962.

Choi, K. and Goldstein, S.A. (1992) A comparison of the fatigue behavior of human trabecular and cortical bone tissue. *J. Biomech.,* **25**:1371-1381.

Choi, K., Kuhn, J.L, Ciarelli, M.J. and Goldstein, S.A. (1989) The elastic modulus of trabecular, subchondral, and cortical bone tissue. *Trans. 35th Orthop. Res. Soc.* **14**:102.

Christiansen, C. (1991) Symposium on osteoporosis: Introduction. *Amer. J. Med.* **Suppl 5B**:1S.

Ciarelli, M.J., Goldstein, S.A., Kuhn, J.L., Cody, D.D., and Brown, M.B. (1991) Evaluation of orthogonal mechanical properties and density of human trabecular bone from the major metaphyseal regions with materials testing and computed tomography. *J. Orthop. Res.* **9**:674-682.

Currey, J. (1984) *The mechanical adaptations of bones.* Princeton University Press, Princeton, NJ.

Daffner, R.H. (1978) Stress fractures: current concepts. *Skeletal Radiol.,* **2**:221-229.

Devas, M.B. (1975) *Stress fractures.* Churchill Livingstone, London.

Ducheyne, P., Heymans, L., Martens, M., Aernoudt, E., Meester, P., and Mulier, J.C. (1977) The mechanical behavior of the intracondylar cancellous bone of the femur at different loading rates. *J. Biomech.*, **10**:747-762.

Dunstan, C.R., Evans, R.A., Hills, E., Wong, S.Y.P., and Higgs, R.J.E.D. (1990) Bone death in hip fracture in the elderly. *Calcif. Tissue Int.*, **47**:270-275.

Evans, F.G., and Lebow, M. (1957) Strength of human compact bone under repetitive loading. *J. Appl. Physiol.*, **10**:127-130.

Fondrk, M., Bahniuk, E., Davy, D.T., and Michaels, C. (1988) Some viscoplastic characteristics of bovine and human cortical bone. *J. Biomech.*, **21**:623-630.

Ford, C.M. and Keaveny, T.M. The shear elastic and failure properties of bovine tibial trabecular bone. *J. Biomechanics*. Submitted 1995.

Forest Products Laboratory (1990) *Wood engineering handbook*. Prentice Hall, Englewood Cliffs, NJ.

Freeman, M.A., Todd, R.C., and Pirie, C.J. (1974) The role of fatigue in the pathogenesis of senile femoral neck fractures. *J. Bone Joint Surg.*, **56B**:698-702.

Ganong, W.F. (1981) *Review of Medical Physiology*. Lange Medical Publications, Los Altos, CA.

Gibson, L.J., Ashby, M.F. (1988) *Cellular Solids: Structure & Properties*. Pergamon Press, New York.

Giladi, M., Milgrom, C., Kashtan, H., Stein, M., Chisin, R., and Dizian, R. (1986) Recurrent stress fracture in military recruits. One-year-follow-up of 66 recruits. *J. Bone Joint Surg.*, **68B**:439-441.

Goldstein, S.A., Hollister, S.J., Kuhn, J.L., and Kikuchi, N. (1990) The mechanical and remodeling properties of trabecular bone. In *Biomechanics of Diarthroidal Joints*, Volume II (Mow, V.C., Ratcliffe, A., and Woo, S.L-Y., eds.). Springer-Verlag, New York, NY.

Goldstein, S.A., Wilson, D.L., Sonstegard D.A., Matthews, L.S. (1983) The mechanical properties of human tibial trabecular bone as a function of metaphyseal location. *J. Biomech.*, **16**:965-969.

Goulet, R.W., Ciarelli, M.J., Goldstein S.A., Kuhn, J.L., Feldkamp, L.A., Kruger, D., Viviano, D., Champlain F. (1988) The effects of architecture and morphology on the mechanical properties of trabecular bone. *Trans 34th Orthop. Res. Soc.* **13**:73.

Gray, R.J., and Korbacher, G.K. (1974) Compressive fatigue behavior of bovine compact bone. *J. Biomech.* 7:287-292.

Griffiths, W.E.G., Swanson, S.A.V., and Freeman, M.A.R. (1971) Experimental fatigue fracture of the human cadaveric femoral neck. *J. Bone Joint Surg.*, **53B**:136-143.

Guo, X.E. (1993) Fatigue of trabecular bone. Ph.D. thesis. Harvard University, Cambridge, MA.

Guo, X.E., Gibson, L.J., McMahon, T.A., Keaveny, T.M., and Hayes, W.C. (1994) Finite element modeling of damage accumulation in trabecular bone under cyclic loading. *J. Biomech.* **27**:145-155.

Hankinson (1921) Investigation of crushing strength of spruce at varying angles of grain. *U.S. Air Service Information Circular* No. 259.

Hipp, J.A., Jansujwicz A.O. (1993) Micro-magnetic resonance imaging of trabecular bone structure. *Trans. 39th Orth. Res. Soc.*, **18**:582.

Hoff, N.J. (1954) Buckling and stability. *J. Royal Aeronautical Society* **58**(517):1-52.

Hull, D. (1981) *An introduction to composite materials.* Cambridge University Press, Cambridge, UK.

Jamison, R.D., Schulte, K., Reifsnider, K.L., Stinchcomb, W.W. (1984) Characterization and analysis of damage mechanisms in tension-tension fatigue of graphite/epoxy laminates. In *Effects of Defects in Composite Materials*, American Society for Testing and Materials.

Jansujwicz, A. (1993) A quantitative study of trabecular bone structure through magnetic resonance micro-imaging. Master's thesis, Boston University, Boston, MA.

Kaplan S.J., Hayes, W.C., Stone J.L., Beaupre G.S. (1985) Tensile strength of bovine trabecular bone. *J. Biomech.* **18**:723-727.

Keaveny, T.M., Pinilla, T.P., Crawford, P., and Wachtel, E.F. (1995) Improved techniques for mechanical testing of human trabecular bone. *Trans. Orthop. Res. Soc.* **20**:530.

Keaveny, T.M., Guo, X.E., Wachtel, E.F., McMahon, T.A., and Hayes, W.C. (1994) Trabecular bone exhibits fully linear elastic behavior and yields at low strains. *J. Biomech.* **27**:1127-1136.

Keaveny, T.M. and Hayes, W.C. (1993) A 20-year perspective on the mechanical properties of trabecular bone. *Trans. ASME* **115**:534-542.

Keller, T.S., Lovin, J.D., Spengler, D.M., and Carter, D.R. (1985) Fatigue of immature baboon cortical bone. *J. Biomech.*, **18**:297-304.

Kelly, A., and Davies, G.J. (1965) The principles of the fibre reinforcement of metals. *Metallurg. Reviews* **10**:1-77.

Krause, G.R. and Thompson, J.R. Jr. (1944) March fracture: an analysis of two hundred cases. *Am. J. Roentg.* **52**:281-290.

Ku, J.L., Goldstein, S.A., Choi, K.W., London, M., Herzig, M.A. and Matthews, L.S. (1987) The mechanical properties of single trabeculae. *Trans. 33rd Orthop. Res. Soc.*, **12**:48.

Kuhn, J.L., Goldstein, S.A., Choi, K.W., London, M., Feldkamp, L.A., and Matthews, L.S. (1989) Comparison of the trabecular and cortical tissue moduli form human iliac crests. *J. Orthop. Res.*, **7**:876-884.

Kuhn, J.L., Goldstein, S.A., Feldkamp, L.A., Goulet, R., Jesion G. (1990) Evaluation of a microcomputed tomography system to study trabecular bone structure. *J. Orthop. Res.*, **8**:833-842.

Lafferty, J.F. (1978) Analytical model of the fatigue characteristics of bone. *Aviation, Space and Environmental Medicine*, **49**:170-174.

Lafferty, J.F. and Raja, P.V.V. (1979) The influence of stress frequency on the fatigue strength of cortical bone. *Trans. ASME J. Biomech. Engr.*, **101**:112-113.

Linde F., Hvid I. (1987) Stiffness behavior of trabecular bone specimens. *J. Biomech.*, **20**:83-89.

Linde F., Hvid I. (1989) The effect of constraint on the mechanical behavior of trabecular bone specimens. *J. Biomech.*, **22**:485-490.

Linde F., Hvid I., Madsen F. (1992) The effect of specimen geometry on the mechanical behavior of trabecular bone specimens. *J. Biomech.*, **25**:359-368.

Lotz, J.C., Gerhart T.N., Hayes, W.C. Mechanical properties of trabecular bone from the proximal femur: a quantitative CT study. *J. Comput. Assist Tomogr.* 14:107-114, 1990.

Matheson, G.O., Clement, D.B., McKenzie, D.C., Tauntan, J.E., Lloyd-Smith, D.R.,

and MacIntgre, J.G. (1985) Stress fracture in athletes: a study of 320 cases. *Am. J. Sports. Med.*, **13**:342-348.

McFarland, P.H. and Frost, H.M. (1961) A possible new cause for aseptic necrosis of the femoral head. *Henry Ford Hosp. Med. Bull.*, **9**:115-122.

Mente, P.L. and Lewis, J.L. (1989) Experimental method for the measurement of the elastic modulus of trabecular bone tissue. *J. Orthop. Res.* **7**:456-461.

Meurman, K.O.A. and Elfving, S. (1980) Stress fractures in soldiers: a multifocal bone disorder. *Radiology,* **134**:483-487.

Michel, M.C., Guo, X.E., Gibson, L.J., McMahon, T.A., and Hayes, W.C. (1993) Compressive fatigue behavior of bovine trabecular bone. *J. Biomech.* **26**:599-607.

Mori, S., and Burr, D.B. (1993) Increased intracortical remodelling following fatigue damage. *Bone* **14**:103-109.

Morris, J.M. and Blickenstaff, L.D. (1967) *Fatigue fracture: a clinical study.* Charles C. Thomas, Springfield, IL.

Nash, C.D. (1966) Fatigue of self-healing structures: A generalized theory of fatigue failure. *ASME Paper*, **66-WA/BHF-3**.

Neter, J., Wasserman, W., Kutner, M. (1990) *Applied linear statistical models.* Irwin Editors, Boston.

Nunamaker, D.M., Butterweck, D.M., and Provost, M.T. (1990) Fatigue fractures in thoroughbred racehorses: Relationships with age, peak bone strain and training. *J. Orthop. Res.,* **8**:604-611.

Odgaard, A., Andersen, K., Melsen, F., Gundersen, H.J.G. (1990) A direct method for fast three-dimensional serial reconstruction. *J. Microscopy.* **159**:335-342.

Odgaard, A., Hvid I., Linde F. (1989) Compressive axial strain distributions in cancellous bone specimens. *J. Biomech.*, **22**:829-835.

Odgaard, A. and Jensen, E.B., and Gundersen, H.J.G. (1990) Estimation of structural anisotropy based on volume orientation. *J. Microscopy*, **157**:149-162.

Odgaard, A. and Linde, F. (1991) The underestimation of Young's modulus in compressive testing of cancellous bone specimens *J. Biomech.* **24**:691-698.

Ohtani, T. and Azuma, H. (1984) Trabecular microfractures in the acetabulum.

Histologic studies in cadavers. *Acta. Orthop. Scand.*, **55**:419-422.

Parfitt, A.M. (1983) The physiologic and clinical significance of bone histomorphometric data. In *Bone Histomorphometry* (ed. Recker, R.R.). CRC Press, Boca Raton, FL.

Paris, P.C. and Erdogan, F. (1963) *Trans. ASME*, **85**:528.

Pattin, C.A. and Carter, D.R. (1990) Cortical bone modulus reduction in tensile and compressive fatigue. *Trans. 36th Orthop. Res. Soc.*, **15**:54.

Pennel, R.G., Maurer, A.H., and Bonakdarpour, A. (1985) Stress injuries of the par interarticularis: radiologic classification and indications for scintigraphy. *Am. J. Roentgenol.*, **145**:763-766.

Pinilla, T.P., Cutler, M.J., Wachtel, E.W., Keaveny, T.M. Comparison of failure properties of bovine proximal tibial trabecular bone for longitudinal and transverse loading. Presented at Orthopaedic Biomechanics Laboratory at Beth Israel Hospital and Harvard Medical School; July 1993; Boston.

Pugh, J.W., Rose, R.M., and Radin, E.L. (1973a) Elastic and viscoelastic properties of trabecular bone: dependence on structure. *J. Biomech.*, **6**:475-485.

Pugh, J.W., Rose, R.M., and Radin, E.L. (1973b) A possible mechanism of Wolff's law: trabecular microfractures. *Arch. Int. Physiol. Biochem.*, **81**:27-40.

Radin, E.L., Parker, H.G., Pugh, J.W., Steinberg, R.S., Paul, I.L., and Rose, R.M. (1973) Response of joints to impact loading. III. Relationship between trabecular microfractures and cartilage degeneration. *J. Biomech.*, **6**:51-57.

Reilly, D.T., and Burstein, A.H. (1975) The elastic and ultimate properties of compact bone tissue. *J. Biomech.*, **8**:393-405.

Schaffler, M.B., Radin, E.L. and Burr, D.B. (1989) Mechanical and morphological effects of strain rate on fatigue of compact bone. *Bone*, **10**:207-214.

Snyder, B.D., Hayes, W.C. Multiaxial structure-property relations in trabecular bone. (1990) In *Biomechanics of Diarthroidal Joints* (Mow, V.C., Ratcliffe, A., and Woo, S.L-Y., eds.). Springer-Verlag, New York, NY.

Swanson, S.A.V., Freeman, M.A.R., and Day, W.H. (1971) The fatigue properties of cortical bone. *Med. & Biol. Engng.*, **9**:23-32.

Todd, R.C., Freeman, M.A., and Pirie, C.J. (1972) Isolated trabecular fatigue fractures

in the femoral head. *J. Bone Joint Surg.*, **54B**:723-728.

Townsend, P.R., Rose, R.M., and Radin, E.L. (1975) Buckling studies of single human trabeculae. *J. Biomech.* **8**:199-201.

Urovitz, E.P., Fornasier, V.L., Risen, M.I., and MacNab, I. (1977) Etiological factors in the pathogenesis of femoral trabecular fatigue fractures. *Clin. Orthop.*, **127**:275-280.

Vernon-Roberts, B., and Pirie, C.J. (1973) Healing trabecular microfractures in the bodies of lumbar vertebrae. *Ann. Rheum. Dis.*, **32**:406-412.

Wong, S.Y., Kariks, J., Evans, R.A., Dunstan, C.R., and Hills, E., (1985) The effect of age on bone composition and viability in the femoral head. *J. Bone Joint Surg.*, **67B**:274-283.

Yoon, H.A. and Katz, J.L (1976) Ultrasonic wave propagation in human cortical bone. I. Theoretical considerations for hexagonal symmetry. *J. Biomech.*, **9**:407-412.

Appendix: High-cycle data from current study

Total	Spec ID #	Applied Load (N)	Resulting Strain Range $\Delta\sigma/Eo$ (%)	Number of Cycles to Fracture (Cf)	Number of Cycles to Failure (Nf)
1	108bl	580	0.54	2442	794
2	spec 15	441	0.53	501	295
3	17cl	280	0.52	4454	194
4	104bl	338	0.45	1957	1935
5	126al	419	0.42	7903	5994
6	63al	455	0.41	2443	2443
7	133hl	340	0.40	923	923
8	130bl	333	0.40	540045	366277
9	27al	357	0.40	96117	29994
10	123bl3	428	0.38	63545	49994
11	22dl	358	0.37	5112	3365
12	9bl	318	0.37	7267	5994
13	54al	275	0.37	10385	10298
14	11dl	205	0.36	18145	18145
15	21al	356	0.36	16717	9994
16	51al	443	0.36	54313	44617
17	132el	341	0.36	17487	17487
18	12bl2	260	0.35	18653	18653
19	2el	360	0.34	17999	17999
20	23al	340	0.34	56173	32686
21	44al	170	0.32	95925	29994
22	48el	111	0.29	320813	319751

Fatigue failure (Nf) was defined as either 10% decrease in initial secant modulus (Eo) or fracture (exceeding the limit on strain channel of 5%).

4903-40